Magmatic and phreatomagmatic contributions on the ash-dominated basaltic eruptions: Insights from the April and November–December 2005 paroxysmal events at Karthala volcano, Comoros

Simon Thivet, Jean Carlier, Lucia Gurioli, Andrea Di Muro, Pascale Besson, Magali Smietana, Georges Boudon, Patrick Bachèlery, Julia Eychenne, Jean-Marie Nedelec

▶ **To cite this version:**

Simon Thivet, Jean Carlier, Lucia Gurioli, Andrea Di Muro, Pascale Besson, et al.. Magmatic and phreatomagmatic contributions on the ash-dominated basaltic eruptions: Insights from the April and November–December 2005 paroxysmal events at Karthala volcano, Comoros. 2022. hal-03578724

HAL Id: hal-03578724
https://uca.hal.science/hal-03578724v1

Preprint submitted on 17 Feb 2022

HAL is a multi-disciplinary open access archive for the deposit and dissemination of scientific research documents, whether they are published or not. The documents may come from teaching and research institutions in France or abroad, or from public or private research centers.

L'archive ouverte pluridisciplinaire **HAL**, est destinée au dépôt et à la diffusion de documents scientifiques de niveau recherche, publiés ou non, émanant des établissements d'enseignement et de recherche français ou étrangers, des laboratoires publics ou privés.

Distributed under a Creative Commons Attribution 4.0 International License

Magmatic and phreatomagmatic contributions on the ash-dominated basaltic eruptions: insights from the April and November-December 2005 paroxysmal events at Karthala volcano, Comoros

Simon THIVET[1,2], Jean CARLIER[2], Lucia GURIOLI[2], Andrea DI MURO[3], Pascale BESSON[4], Magali SMIETANA[2], Georges BOUDON[4], Patrick BACHELERY[2], Julia EYCHENNE[2,5], Jean-Marie NEDELEC[6]

(1) Department of Earth and Environmental Sciences, Ludwig-Maximilians-Universität, München, Germany

(2) Laboratoire Magmas et Volcans, Université Clermont Auvergne - CNRS - IRD, OPGC, Campus Universitaire des Cézeaux, 6 Avenue Blaise Pascal, 63178 Aubière Cedex, France

(3) Université de Paris, Observatoire Volcanologique du Piton de la Fournaise, Institut de Physique du Globe de Paris, CNRS, F-97418, La Plaine des Cafres, La Réunion, Paris, France

(4) Institut de Physique du Globe (IPGP), Sorbonne Paris-Cité, CNRS UMR-7154, Univ. Paris Diderot, 1 rue Jussieu, 75238 Paris, France

(5) GReD, Université Clermont Auvergne, CNRS, INSERM, Clermont-Ferrand, France

(6) Université Clermont Auvergne, CNRS, SIGMA Clermont, ICCF, F-63000 Clermont-Ferrand, France

Corresponding author: Simon Thivet, simon.thivet@lmu.de

Abstract

Basaltic eruptions are commonly associated with lava emissions and relatively weak explosive activities, but they can sometimes produce strong explosive eruptive phases. In April and November 2005, two paroxysmal eruptive events occurred within the summit crater of Karthala basaltic shield volcano (Grande Comore Island, Comoros), which hosted a water lake before each of these events. Both 2005 ash plumes spread across the Comoros Archipelago and heavily impacted the whole Grande Comore Island. Associated deposits on the volcano summit are extremely fine-grained (up to 50 wt% of fine ash < 63 μm for some analyzed layers) and rich in millimeter-sized rounded accretionary lapilli aggregates. Field observations, as well as textural and chemical analyses performed on both coarse- and fine-grained pyroclasts permit to identify juvenile and non-juvenile

components and quantify their peculiar characteristics. Coarse ash (710-1000 µm) mainly consists of juvenile pumice particles (vesicle number density N_V = 4.5 10^4 mm^{-3} and gas to melt ratio V_G/V_L = 1.5, on average), characterized by free groundmasses and representative of magma portions ascending quickly within the eruptive conduits (up to 10 m s^{-1}). A relatively low amount of juvenile scoria particles are also observed in the coarse ash fractions, which are characterized by magma degassing (N_V = 4.7 10^4 mm^{-3} and V_G/V_L = 0.5 on average) and associated crystallization (occurrence of dendritic microlites). Non-juvenile fragments (from blocks to coarse ash) are dense lava or intrusive fragments. Their amount decreases exponentially toward the fine ash fractions, which are mainly composed of juvenile, blocky, dense and glassy particles that are characterized by unambiguous textural signs of brittle fragmentation (hackle lines, stepped features and cracks). We support that Molten Fuel-Coolant Interactions between highly porous fast ascending basaltic magmas and external waters occurred during the paroxysmal phases of the studied eruptions, leading to a brittle-dominant and efficient regime of magma fragmentation. Variable but large amount of fine ash grains through the stratigraphic depth of the deposits can be ascribed to the brittle failure of the vesicle walls of the initial porous magma. Concurrently, thermohydraulic explosions caused the host rock fragmentation at shallow level, generating the relatively coarse non-juvenile particles. A short-lived episode of intense lava fountaining associated with steam explosions eventually occurred at the end of the November 2005 paroxysm, forming the last and relatively coarse tephra layer at the top of the studied eruptive sequence. Each paroxysmal phase lasted about a day as each associated water lake and shallow water table progressively vaporized and dried away. Both eruptions ended with lava pond and weak lava fountaining activities confined within the summit crater. We conclude that the contributions of both magmatic processes and phreatomagmatic interaction mechanisms ultimately generated the grain size, grain component and grain texture variabilities observed within the paroxysmal deposits. This work contributes to a better understanding of the generation of unusual fine ash from basaltic explosions as well as their eruptive dynamics and associated mechanisms, from magma ascent in the conduit to the fragmentation level and the interaction with intra-crateric lake waters.

Keywords

Ash; basaltic; Karthala; Comoros; phreatomagmatism; texture

Highlights

- Karthala basaltic volcano produced two paroxysmal events in 2005
- Associated fallout deposits were highly spread out and rich in fine ash
- Tephra deposits record the signatures of shallow water-magma interactions
- Phreatomagmatism enhanced host rock and magma fragmentation efficiencies

1. Introduction

Volcanic activity represents an important part of natural hazards and risks on Earth (Small and Naumann, 2001). Active basaltic volcanism is widespread, present in all tectonic contexts, and is usually associated with effusive as well as weak explosive events from Hawaiian-like to Strombolian-like activities (Siebert et al., 2015). Low magma viscosities and low magmatic volatile contents (Taddeucci et al., 2015) ultimately lead to low efficiency fragmentation mechanisms when the magma is emitted at the surface, typically forming lava flows and relatively coarse-grained tephra (Cashman and Scheu, 2015). Many studies on active basaltic volcanoes highlight this common volcanic behavior, for instance at Piton de la Fournaise (e.g., Gurioli et al., 2018; Edwards et al., 2020; Thivet et al., 2020b), Stromboli (e.g., Gurioli et al., 2014; Gaudin et al., 2017; Thivet et al. 2021), Etna (e.g., Polacci et al., 2006; Andronico and Corsaro, 2011; Vergniolle and Gaudemer, 2012), as well as for Hawaiian (e.g., Head and Wilson, 1987; Stovall et al., 2011; Parcheta et al., 2013) and Icelandic volcanoes (e.g., Thordarson and Larsen, 2007; Pedersen et al., 2017; Bonny et al., 2018).

However, eruptive intensity can fluctuate, even during a single eruption, paroxysmal phases/events corresponding to the moments of greatest intensity. Basaltic volcanism can indeed shift toward more intense activities from Strombolian (Pioli et al., 2008) to sub-Plinian (Jordan et al., 2016) and Plinian-like (Costantini et al., 2010).

Basaltic paroxysmal events can be due to specific magmatic processes such as fast ascent of deep volatile-rich primitive magma (Métrich et al., 2010), gas transfer from deep to shallow levels resulting in destabilization of the upper magma column (Aiuppa et al., 2010), plug pressurization resulting in intermittent decompressions of the upper system (Thivet et al., 2020a), syn-eruptive magma degassing and crystallization resulting in the drastic increase of the magma viscosity in the volcanic conduit (Giordano and Dingwell, 2003) and sudden tectonic events such as caldera collapse resulting in secondary tephra fragmentation (Thivet et al., 2020c).

Moreover, magmas or lavas can also interact with external fluids at different levels (e.g. intra-crateric lake waters, fluids from hydrothermal systems, ocean) resulting in the so-called hydrovolcanism, which can lead to relatively explosive behaviors, as during phreatic or

phreatomagmatic activities (e.g., Mastin and Witter, 2000; Belousov and Belousova, 2001; Graettinger et al., 2013; Houghton et al., 2015; White et al., 2015; Zimanowski et al., 2015; Németh and Kósik, 2020). This kind of activities is reported for several basaltic systems, such as Piton de la Fournaise (e.g., Staudacher et al., 2009; Michon et al., 2013; Thivet et al., 2020c), Hawaii (e.g., McPhie et al., 1990; Dvorak, 1992; Dzurisin et al., 1995) and Iceland (e.g., Dellino et al., 2012; Gudmundsson et al., 2012; Magnússon et al., 2012).

The large range of possible scenarios associated with basaltic explosive activity makes the related hazards and associated risks difficult to anticipate. With respect to weak intensity basaltic volcanism (e.g. lava flows, Hawaiian fountaining and mild Strombolian explosions; Thivet et al. 2020b), paroxysmal basaltic events are more impactful mainly because of the emission of large amounts of fine-grained tephra, which can disperse over large areas (Jenkins et al., 2015). This is a critical point for awareness and anticipation of such volcanic crises as well as for hazard assessment (Nassor, 2001; Morin et al., 2016).

In the present study, we focus on two distinct paroxysmal basaltic phases of the Karthala shield volcano (Grande Comore Island, Comoros, Fig. 1) producing large plumes and regionally dispersed ash-rich deposits, in April and November 2005. Hazards associated with both paroxysms impacted most of the Grande Comore Island (Bachèlery et al., 2016): projections of ballistics were reported within the summit uninhabited area of the volcano, while significant ash fallouts and associated mudflows spread downslope within inhabited areas, including in Moroni, the capital of Comoros. Here, we summarize the morphological and eruptive history of the volcano in the last 30 years and present the results of a detailed textural study of the ash-rich fallout deposits the both 2005 paroxysms. These deposits are also compared with more typical Hawaiian-like deposits, in particular that from the 1977 eccentric eruption that occurred at low altitude on the southwestern flank of Karthala volcano. A chemical overview is also addressed in order to contextualize the compositions of the emitted magmas during the recent activity of the volcano. All these insights are discussed in order to constrain the syn-eruptive dynamics of the studied eruptions, in terms of reservoir, conduit processes and fragmentation mechanisms as derived from pre-, syn- and post-eruptive observations, as well as from features of the investigated deposits.

2. Geological context

2.1. Comoros archipelago

Karthala volcano is located on the Grande Comore (or Ngazidja) Island, which is the westernmost island of the Comoros archipelago that is formed by four main volcanic islands (from West to East: Grande Comore, Mohéli, Anjouan and Mayotte) in the northern part of the Mozambique Channel (Fig. 1a). The tectonic setting and the origin of the Comoros archipelago is the subject of controversy (e.g., Flower and Strong, 1969; Emerick and Ducan, 1982; Nougier et al., 1986) but recent tectonic and geomorphological measurements rule out the presence of a hotspot and interpret the Comoros archipelago as the boundary between two tectonic plates, favoring upwelling of mantellic magmas (Famin et al., 2020; Tzevahirtzian et al., 2021). Magnetic data support the presence of oceanic crust in this area (Coffin and Rabinowitz, 1987), which is also compatible with sedimentary and tectonic arguments to explain the presence of detrital crustal rocks in the area as well as abundant sandstone enclaves within the Comorian lavas. The Comorian volcanism started in Mayotte around 20 Ma, emitting a wide range of alkaline and variably undersaturated (from basanite-tephrite up to phonolite) magma compositions and forming a wide range of eruption styles, as evidenced by the variability of deposits and edifice morphologies in the archipelago (Bachèlery et al., 2016; Michon, 2016; Tzevahirtzian et al., 2021).

2.2. Grande Comore Island and Karthala volcano

Karthala basaltic shield volcano is the largest emerged active volcano of the area (Bachèlery et al., 2016). It represents one of the two recently active Comorian volcanic systems, with the newly formed submarine volcano of Mayotte (e.g., Cesca et al., 2020; Lemoine et al., 2020; Feuillet et al., 2021). Karthala (summit at 2361 m above sea level) forms the southern two-thirds of the Grande Comore Island, while La Grille volcano (summit at 1087 m above sea level) forms the northern part of it (Fig. 1b). A third and old massif, named M'Badjini, has also been identified in the southernmost part of the Island (Bachèlery and Coudray, 1993; Bachèlery et al., 2016). Karthala eruptions are mostly effusive and associated with weak explosive activities (lava fountaining and mild Strombolian explosions), although explosive events have usually occurred as shown by the alternation of lavas and pyroclastic deposits on the summit crater walls. Products are mainly alkaline basalts (Bachèlery and Hémond, 2016) that usually contain olivine, clinopyroxene and more rarely plagioclase phenocrysts.

The summit area of Karthala volcano corresponds to the junction of two well-defined rift-zones and hosts a remarkable caldera complex (Strong and Jacquot, 1970; Poppe, 2012) which is 3.5 km long and 2.8 km wide (Fig. 1c). The presence of several collapse structures, scattered craters and pit craters of different sizes within the summit area, suggests that several shallow magmatic reservoirs feed the volcano summit activity. Geophysical investigations (Lénat et al., 1998; Savin et

al., 2001, 2005; Bernabeu et al., 2018) have permitted to define the structure of the summit area, which can be schematically divided in three main units: (i) an upper 200-400 m thick sequence of dry basaltic rocks, (ii) an intermediate 300 to 1200 m thick water-saturated unit and (iii) a deep conductive unit hosting the hydrothermal system. The second unit forms the ground water body whose surface expression was the Choungou-Chahalé intra-crateric lake (visible each of the 2005 eruptions), while the deeper hydrothermal system is better developed below the northern caldera lobe where is located the Changou-Chagnoumeni pit-crater.

2.3. Recent eruptive activity and summit morphology evolution of Karthala volcano

According to the observations of the inhabitants of the Grande Comore Island, Karthala erupted at least 15 times during the 20th century (Bachèlery et al., 2016). In April 1977, an eccentric magmatic eruption occurred at low altitude (around 390 m above sea level) on the southwest flank of the volcano, producing lava fountains and lava flows, which invaded the adjacent villages of Singani and Hetsa, and which attained the coastline (Krafft, 1982). Then, and since the creation of the Karthala Volcanological Observatory (OVK) in 1988, five summit eruptions occurred in July 1991, April 2005, November-December 2005, May-June 2006 and January 2007, which all took place within the Choungou-Chahalé crater, except the 2007 one, which took place within the Choungou-Chagnoumeni pit-crater (Fig. 1c). Mainly due to these volcanic events, the morphology of the summit area has frequently changed (Fig. 2). Bachèlery et al. (2016) detailed the pre- and syn-eruptive phases of each of these recent eruptions and the following paragraph summarizes the most important points derived from that study.

After the one-day, July 11, 1991 phreatic eruption (Bachèlery et al., 1995; Savin et al., 2005), a new crater formed (around 280 m in diameter and 40 m in depth) and was rapidly filled by an intra-crateric water lake that regularly changed in terms of water level and color, probably indicating acidity changes (Fig. 2a). The first precursors of the April 2005 eruption were recorded by mid-2003, characterized by a progressive increase in the seismic activity. The eruption (Fig. 2b) began on April 16, on the same location of the lake, after a seismic crisis of three hours (drastic increase of the volcano-tectonic earthquakes frequency). The initial paroxysmal phase of the eruption was characterized by the emission of a gas-rich and ash-rich plumes associated with the projections of ballistics. During this phase, which lasted until the night between April 17 and April 18, rumbles, volcanic lightning, sulphur smell and mudflows were reported by several coastal villages (Morin et al., 2009). Most importantly, the two thirds of the island were covered by ash due to heavy ash fallouts. From April 18, the main explosive activity stopped, revealing that the lake disappeared and was replaced by an active lava pond associated with weak lava fountaining, which progressively in

intensity until the end of the eruption on April 19. A water lake formed again in the Choungou-Chahalé crater around May 8. Between May and November 2005, seismicity rates were oscillating, and a new eruption began on November 24 within the Choungou-Chahalé crater (Fig. 2c). As during the April eruption, the initial phase was characterized by the emission of a large plume, which reached the altitude of 12 km above sea level, with a lateral East-West extension over the whole Comoros archipelago. During the first day of the eruption, heavy ash falls obscured sunlight over half part of Grande Comore Island. The paroxysmal phase ended on November 25, again revealing that the lake disappeared and was replaced by an active lava pond at the bottom of the crater associated with weak lava fountaining, which progressively decreased in intensity until the end of the eruption on December 8. In total, these two similar eruptions affected around 250,000 people, mainly because of syn-eruptive ash fallouts and significant SO_2 emissions (Prata and Kerkmann, 2007) that affected aviation safety, air quality and drinking water resources (Morin et al., 2009; 2016). Syn- and post-eruptive mudflows caused a lot of disruption as well (Dille et al., 2020). A few centimeters of ash accumulated on the coast, while the summit area was covered by several meters of pyroclastic deposits (Smietana, 2007) made of blocks, bombs and ash (Fig. S1). After the November-December 2005 eruption, the intra-crateric water lake has not returned. In May 2006, an increase in seismicity was recorded again. On May 28, approximately after two hours of seismic crisis, a new magmatic eruption started within the Choungou-Chahalé crater (Fig. 2d). The eruption was characterized by lava fountains, reaching 50 meters in height and forming a lava pond inside the crater, which caused no major threat to the population. The lava pond progressively cooled down until the end of the eruption on June 1 and raised up the crater floor by approximately a hundred meters. Finally, a one-day magmatic eruption occurred on January 13, 2007, within the Choungou-Chagnoumeni pit-crater (Fig. 1c), which was entirely filled by lava at the end of the eruptive activity (Bernabeu et al., 2018). This latter eruption ended a three-year cycle of notable activity. The current morphology of the summit area of Karthala volcano results from these recent eruptive events as well as constant erosion (Fig. 2e).

3. Methods

3.1. Field work and sampling

Samples from 1977, April 2005, November-December 2005, May-June 2006 and January 2007 eruptions were collected during several field expeditions performed in November 2006, April 2007 and October 2018 (Table S1).

Concerning both 2005 eruptions, several stratigraphic logs were excavated and described within or near the summit caldera complex, 500 to 1500 meters from the center of the Choungou-Chahalé crater (Fig. 1c). Six logs were described in detail in November 2006 (annotated KAR_5, KAR_9, KAR_10, KAR_15, KAR_17 and KAR_18) and two others were added in October 2018 (annotated KAR_2005a and KAR_2005b). In addition, 185 measurements of deposit thickness were realized within 10 km^2 in the summit area of the volcano to constrain ash dispersal and volumes and to characterize the lateral facies evolution of both 2005 eruptions (Table 1, Fig. S1). KAR_10 log (Figs. 3a and 3b), of 130 cm in thickness, represents the best sequence of the whole fallout deposits representative of both April and November 2005 paroxysms. Within this log, each identifiable layer (identified thanks to grain size and color changes, annotated with letters from KAR_10_a to KAR_10_u) was carefully sampled and analyzed. In addition, the very last identifiable deposit of the November 2005 paroxysm was also collected from the more proximal outcrop (KAR_2005b), for a total of 22 collected samples. The other logs were described and used to (i) better distinguish and extrapolate the limit between the April 2005 and the November 2005 deposits, (KAR_5, Fig. S2), (ii) observe the distal, medial and proximal deposit facies and measure thickness variations (KAR_9, KAR_15 and KAR_17 respectively, Fig. S3), (iii) identify surge deposits that were also locally emplaced during the eruptions (KAR_18, Fig. S4). , (iv) represent the heterogeneity and main features of the medial to proximal fallout deposit facies (KAR_2005a, Fig. S5) and (v) complete the sampling for chemical analysis. Eruptive products from the lava pond and associated weak explosive lava fountain activities of both April and November-December 2005 eruptions were unfortunately inaccessible due to their low dispersion (mainly falling and recycling into the active lava pond).

Proximal bombs and lapilli from the magmatic May-June 2006 and January 2007 eruptions were collected near their respective vents (KAR_2006 and KAR_2007 respectively, Fig. 1c), in November 2006 and April 2007 respectively. In October 2018, the purely magmatic lava fountain deposits of the 1977 eccentric Singani eruption (KAR_1977_a and KAR_1977_b) were collected 100 m far from the corresponding eruptive vent (Figs. 1b and S6), in order to be compared with the 2005 ash-rich paroxysmal deposits of the summit activity. All the samples were systematically dried in the oven at 70°C for 48 hours. This low temperature drying step preserved any potential phases present on the samples, eased the manual sieving and allowed to perform accurate density measurements (Ross et al., 2022).

3.2. Grain size analysis

Grain size analysis was performed on the two pyroclastic samples of the 1977 eruption (KAR_1977_a and KAR_1977_b samples) as well as on all pyroclastic samples of the both 2005

paroxysms (samples that belong to the KAR_10 log and KAR_2005b sample), using both manual sieving (above 22 µm in intermediate diameter using sieves each ½ ϕ) and laser diffraction measurements (below 45 µm, with a detection limit of 0.1 µm in equivalent diameter) for fine ash-rich samples, following the Eychenne et al. (2012) and Thivet et al. (2020c) procedures. Accretionary lapilli (when occurring) were gently dismantled beforehand. The overlap between 22 and 45 µm for the two techniques was used to fit both results, in order to quantify representative particle size distributions for the whole eruptive sequences (Table S2). Traditional millimeter and phi scales were used to describe the deposit grain sizes, both being linked by this equation: $\phi = -\log_2(d)$, with d the particle grain size in mm (Taner, 1969).

3.3. Tephra component and ash morphology analyses

Pyroclast components were identified and quantified in the same samples as the grain size analysis and for different grain size fractions (Table S3), in order to distinguish juvenile (material representative of the magma feeding the eruptions) and non-juvenile (material representative of pre-existing fully solidified lithic rocks that are expulsed/fragmented during the eruptions) particles (White and Houghton, 2006). This distinction was based on the color, surface texture, morphology, porosity, crystal content and assemblage of the particles. Particle counting was performed on a selection (based on sample quantity and quality) of ½ ϕ grain size fractions previously isolated by sieving. Lapilli (when occurring) were systematically counted for each layer by hand and using a binocular microscope. Selected ash fractions between 500 µm and 2 mm were counted using a binocular microscope. Selected ash fractions below 500 µm were embedded in epoxy resin and then polished. These ash particles were then counted using a JEOL JSM-5910 LV scanning electron microscope (SEM), acquiring back-scattered electron (BSE) images with an acceleration voltage of 15 kV. For all analyzed layers and analyzed grain size fractions, at least 500 particles were counted (when enough were available), in order to perform a statistically representative counting following the Van der Plas and Tobi (1965) statistic rules.

Ash morphology measurements, which correspond to an apparent projected shape of ash (APASH), were performed using the automated Malvern Morpho-Grainsizer Morphologi G3 following the method developed by Leibrandt and Le Pennec (2015) and adapted by Thivet et al. (2020c). In total, 20979 particles were analyzed (Table S3) with different magnification (from x2.5 to x20 depending on the analyzed grain sizes), allowing the representative quantification of several particle shape parameters: solidity (SLD), convexity (CVX), sphericity (SPH) and aspect ratio (AR) parameters are specifically discussed in this study, respectively representing the morphological roughness (mostly based on the particle area), the textural roughness (mostly based on the particle perimeter),

289 the angularity (based on both particle area and perimeter) and the elongation (ratio between the
290 particle width and length) of the measured particles (specific definitions and formulas can be found
291 in the previously cited studies). Ash morphology measurements were performed on different grain
292 fractions, almost covering the whole range of ash sizes from 63 to 1400 µm (loss of analytical
293 precision below and above this range), for some 2005 paroxysmal layers (KAR_10_a, b, c, j, k, l, n and
294 o; Carlier, 2019) as well as a layer from the 1977 eruption (KAR_1977_a).

295 **3.4. Textural analyses**

296 Textural analyses of tephra particles were then performed using several techniques. The
297 different components identified were analyzed distinctly. For each component, several tephra layers
298 have been selected based on sample quality and quantity. First, 3D images were acquired on coarse
299 (710-1000 µm) and fine (< 63 µm) grain size fractions, using a Zeiss-Supra 55VP Gemini Column field
300 emission scanning electron microscope (FE-SEM) and acquiring secondary electron (SE) images with
301 an acceleration voltage of 3 kV. All the acquired 3D images are shown in Fig. S7 (98 images in total,
302 performed on KAR_10_c, k, l, n, o, p, t, KAR_2005b and KAR_1977_a samples). These images allowed
303 to identify specific textural features on the particle surfaces for the different identified components.

304 Then, 2D images were also acquired using the JEOL JSM-5910 LV SEM, in BSE mode with an
305 acceleration voltage of 15 kV, in order to investigate the internal textures of the ash particles. For
306 each juvenile sample, the vesicle density number (N_V), the vesicle to melt ratio (V_G/V_L), the vesicle
307 size distribution (VSD) and the total porosity fraction were reconstructed in 3D and quantified (Table
308 S4) following the procedure adapted by Thivet et al. (2020b) and measuring about a thousand
309 vesicles (equivalent to around seven ash particles on the 710-1000 µm grain size fraction), in order to
310 perform a statistically representative vesicle count (Van der Plas and Tobi, 1965). The acquired 2D
311 images as well as their corresponding binarized counterparts are shown in Fig. S8 (68 images in total
312 performed on KAR_10_a, b, c, l, n, o, KAR_2005b and KAR_1977_a samples). Crystal contents are not
313 quantified (due to their scarcity and/or relatively small sizes in some of the components) but
314 qualitative observations on crystallinity is nevertheless shown, compared and discussed in this study.

315 Density and derived porosity, as well as connected porosity (vesicle connectivity)
316 measurements (Table S4) were performed on 31 lapilli fragments from the 1977 eruption
317 (KAR_1977_a and b samples) and both 2005 paroxysms (KAR_10_b, c, g, i, s and KAR_2005b
318 samples), following the procedure adapted by Thivet et al. (2020b). (i) Clast density measurements
319 were performed using a Micromeritics Geopyc 1360 envelope density analyzer, (ii) porosity was
320 derived using a vesicle-free rock density of 2874 kg m^{-3}, which was determined by powdering four
321 lapilli fragments (from KAR_10_a and KAR_2005b samples) and by measuring their masses and

volumes using the Micromeritics Accupyc 1340 helium pycnometer. (iii) This pycnometer was also used to determine the skeletal volumes of the samples in order to calculate the connected porosity for each corresponding clast.

3.5. Chemical analyses

Analyses of bulk rock composition as well as in situ matrix and mineral chemistry (Table S5) were performed on selected clasts from the 2005, 2006 and 2007 eruptions (Smietana, 2007).

For bulk rock analyses, each selected sample (bombs or lapilli from KAR_10_c, I, s, KAR_17, KAR_2006 and KAR_2007 samples) was powdered and dissolved in acid solutions. The final solutions were analyzed using a Horiba Jobin-Yvon Ultima C inductively coupled plasma atomic emission spectrometer (ICP-AES) for major elements analysis and using an Agilent 7500 quadrupole inductively coupled plasma mass spectrometer (ICP-MS) for rare earth element (REE) analysis. One additional bulk lava composition from the 1977 eruption has also been added from Desgrolard (1996) for comparison.

In situ measurements of matrix (glass) and mineral chemistry were performed on representative samples (KAR_10_c, s, KAR_2006 and KAR_2007) using a Cameca SX100 electron probe micro-analyzer (EPMA), with an acceleration voltage of 15 kV and a current intensity of 10 nA. A 10 µm beam and a focused beam were used for the glass and crystal analyses, respectively.

In addition to these analyses, mineral phases on the 1977 (KAR_1977_a) and both 2005 paroxysmal (KAR_10_f, t and KAR_2005b) ash deposits were identified by X-ray diffraction (XRD) analysis (Table S5), using an Empyrean diffractometer, operated at 43 kV and 38 mA, following a method described in Thivet et al. (2020c). Qualitative Energy-dispersive X-ray spectroscopy (EDXS) spectrums were also acquired on some ash surfaces from both 2005 eruptions (KAR_10_c, p and t), in order to identify potential secondary phases from the primary ash surface backgrounds, using the Zeiss-Supra 55VP Gemini Column FE-SEM, with an acceleration voltage of 15 kV (Table S5).

4. Results

4.1. Fallout deposit features and grain size characteristics

Despite heavy rain falls and strong winds that caused constant soil erosion, the April and November 2005 deposits were still well preserved during the 2006 and 2018 field campaigns, both inside the summit Karthala caldera complex and on its outer proximal slopes. Their thickness and grain size drastically increase when moving towards the eruptive vent. Juvenile bombs and non-

juvenile blocks (from a few cm to a meter in equivalent diameter) are also very abundant in the proximal areas (Figs. 2e, S1 and S3c). Eruptive deposits sampled within the KAR_10 log, which is the most complete stratigraphic log of the April and November 2005 fallout deposits (Figs. 3a and 3b), are located towards the northwest and 500 m of distance from the Choungou-Chahalé crater rim, which corresponds to a medial area (intermediate deposit thickness, absence of bombs and blocks and absence of cross-stratified surge deposits that are mainly visible in the northwestern part of the caldera, cf. Fig. S4). At this location, the April and November deposits are respectively 70 and 60 cm thick, with 12 (from KAR_10_a to KAR_10_l) and 10 (from KAR_10_m to KAR_10_u with also KAR_2005b) identifiable and sampled layers, respectively. Each layer has a constant lateral thickness ranging from a minimum of 1 (KAR_10_e) up to 17 cm (KAR_10_f) within the April 2005 deposits, whereas in the November 2005 deposits the variation ranges from 3 (KAR_10_m) to 12 cm (KAR_10_t). Most of the layers, especially the fine-grained ones (e.g., KAR_10_d, f, h, p, r, and t), are enriched in millimeter-sized rounded accretionary lapilli.

Grain size parameters of each layer are represented in Fig. 3c, which reveal the dominantly fine-grained characteristics of the 2005 paroxysmal deposits, whose sorting values range between 1 and 3 ϕ and whose grain size mean range between 32 and 500 µm, except for the last emitted products of November (KAR_2005b) that represent the coarsest tephra layer (grain size mean of 4 mm) of all 2005 beds. In the whole sequence, 16 layers show unimodal grain size distributions (main modes ranging from 31 to 1000 µm), whereas 6 are bimodal (finer modes ranging from 31 to 90 µm and coarser modes ranging from 250 to 1400 µm). The coarsest grains are 1.6 cm in diameter (except for the KAR_2005b sample, which contains clasts up to 3.2 cm in diameter) and most importantly, 15 layers contained fine ash particles as fine as 1 µm.

April and November 2005 paroxysmal deposits are much finer-grained than the 1977 typical magmatic deposit (Table S2), which is characterized by unimodal grain size distributions (modes between 4 and 8 mm), the coarser grains being 22.6 cm in diameter and lacking particles finer than 45 µm (grain size mean values at 5.66 mm).

4.2. Tephra grain components and associated characteristics

Four main tephra components are identified in each sampled layer of the April and November 2005 deposits: (i) coarse juvenile pumice (Fig. 4), (ii) juvenile scoria (Fig. 5), (iii) non-juvenile (Fig. 6) and fine juvenile dense glassy (Fig. 7) grains. They are described hereafter based on the observations made on coarse (lapilli and coarse ash in the 710-1000 µm grain size fraction) and fine ash (< 63 µm) grain size fractions. Juvenile vs. non-juvenile component distributions as a function of grain size (Fig. 8) as well as ash morphological features (Fig. 9) are also described.

4.2.1. Juvenile pumice grains

Juvenile pumice grains are characterized by a yellow and shiny color, well-visible on the lapilli-sized clasts, whose surfaces are often characterized by bread-crusted cracks (Figs. 4a and 4b). They have also characterized by a pumiceous matrix. Scarce (< 5 vol%) micro-phenocrysts (up to 200 µm in length) of olivine, clinopyroxene and plagioclase are observed in some lapilli clasts and rare loose crystals are present in the ash fraction. SEM images of the coarse ash fraction reveal that pumice grains can either have sub-rounded shapes with no broken angular surfaces (Fig. 4c) or can have some broken angular surfaces characterized by the occurrence of microscopic hackle lines, stepped features and branching quench cracks (Fig. 4d). Pumice ash particles are also characterized by the scarcity of both micro-phenocrysts and microlites, hence are mainly composed of glass and vesicles, which can be rounded (spongy texture, Figs. 4c and 4e), elongated (tube pumice texture, Fig. 4d), or highly deformed (shrinkage texture, Fig. 4f) with often thin vesicle walls (around 1 µm) that can be sometimes broken (Fig. 4g). Highly fluidal, Pele's hairs and tears are not observed in the 2005 deposits.

As a comparison, the 1977 magmatic deposit (Fig. S6) is composed of fluidal (with Pele's hairs and tears) particles, characterized by a slightly lower content of vesicles and slightly higher content of microlites than the 2005 juvenile pumice grains. The 1977 ash grains do not show any significant angular faces, with no cracks and stepped features (Fig. S7). Moreover, these particles do not show any significant deformation features such as vesicle shrinkage or breakage, contrary to some of the 2005 ash particles.

4.2.2. Juvenile scoria grains

Juvenile scoria lapilli grains are characterized by spiny and rough surfaces without any significant cracks and bread-crusted features, as well as by dark/mat colors and by less abundant vesicles than their pumiceous counterparts (Figs. 5a and 5b). Their low content in micro-phenocrysts (< 5 vol%) is similar to those of pumice grains. SEM images of the coarse ash fraction highlight that scoria grains have irregular and rough shapes (Fig. 5c). These scoria grains are also characterized by a variable content in microlites (from around 5 vol% to a fully crystallized matrix, representing sideromelane to tachylite textures) accompanied with a decrease in vesicle abundance compared to the pumice grains. Microlites (up to 20 µm in length) are sometimes protruding from the grain surfaces (Fig. 5d) suggesting tachylitic textures. Microlites are made of plagioclase, clinopyroxene, olivine and Fe-Ti oxides (in order of abundance) and have dendritic textures. The higher the microlite content, the more coalesced the vesicles (Figs. 5e, 5f and 5g).

4.2.3. Non-juvenile grains

Non-juvenile grains are dense and characterized by blocky shapes (Figs. 6a, 6b and 6c). These grains are sometimes partially embedded in vesicular juvenile melt (Figs. 6d and 6e) and show variable crystallized textures, from tachylite (rapid crystallization textures that could correspond to ancient lavas, Fig. 6f) to micro-gabbro (relatively slow crystallization texture that could correspond to plutonic rocks, Figs. 6g and 6h), with the occurrence of plagioclase, clinopyroxene and olivine crystals as well as oxides from 10 to 200 µm in length (Figs. 6e, 6f, 6g and 6h). Note that rare micro-gabbroic enclaves containing interstitial melt in between their own crystals also occur inside coarse juvenile fragments (Fig. 6i). Hence, we suggest that these enclaves represent crystallized parts of the involved magmatic chamber and are thus considered as juvenile material.

4.2.4. Fine ash characteristics

The fine ash (< 63 µm) grains include the three components previously described except that the coarse juvenile pumice component is replaced by the fine juvenile dense glassy one (Fig. 7a). Accretionary lapilli aggregates are omnipresent in the fine-grained layers of both April and November 2005 deposits and are mainly composed of fine ash particles, with some scarce coarse ash grains, the coarser ones being in the inner parts and the finer ones being on the outer rims (Fig. 7b). Contrary to the relatively coarse-grained juvenile pumice grains that are glassy and highly vesicular (Fig. 4), the corresponding fine-grained particles are glassy but dense, with scarce < 50 µm vesicles (Figs. 7a and 7b) and are characterized by ubiquitous microscopic hackle lines and stepped features with scarce branching quench cracks on their surfaces (Figs. 7c, 7d, 7e, 7f, 7g, 7h and S7). Hackles lines are characterized by repeated irregularities that are parallel to sub-radial on the broken faces of the particles. The length of these irregularities does not exceed 40 µm and are repeated every 1 to 10 µm. The stepped features yield irregular particles with an uneven surface made up of three-dimensional polyhedral elements. The branching quench cracks are fracture networks within fresh glass. SEM images also highlight the occurrence of many very fine particles down to 0.1 µm on the surface of the fine ash particles (these very fine particles are not visible on the grain size measurements because of their relatively low masses and volumes). Some particles are also characterized by secondary thin mineral depositions on their surface (< 1 µm thin), which could not be clearly identified by EDXS analysis in term of chemical composition (Table S5). Most importantly, the juvenile dense glassy grains undoubtedly dominate the fine ash grain size fractions compared to both non-juvenile (corresponding to loose crystal fragments) and juvenile scoria grains.

XRD measurements performed on the fine ash fractions (< 45 µm) of KAR_10_f and KAR_10_t samples show similar results as the measurements performed on coarser ash fractions (250 to 355 µm) of KAR_10_f (April 2005 paroxysm), KAR_10_t and KAR_2005b (November 2005 paroxysm), as

well as KAR_1977a (1977 eruption) samples: only typical magmatic phases are detected among with plagioclase, clinopyroxene, rhönite, olivine, and Fe-Ti oxide in order of average abundance (Table S5), with the notable absence of hydrothermal phases. The analyzed ash sample from the 1977 eruption (KAR_1977a, 250 to 355 µm) show a higher content of olivine than in the 2005 products, in accordance with the optical observations.

4.2.5. Ash components and morphologies

Juvenile vs. non-juvenile component proportions have been determined within all April and November 2005 layers and within different grain size fractions. No significative differences are observed between the different analyzed layers (Table S3). However, the component proportions significantly vary with the grain size (Fig. 8) for all the layers. Non-juvenile grains occur mostly within the coarser grain size fractions, with a juvenile grains/non-juvenile grains ratio of 1 within the 22.6-32 mm grain size fraction, on average. The ratio is then oscillating at low values (between 1 and 7, on average) for grain size fractions between 32 mm and 500 µm. From 500 µm and towards fine-grained fractions, the ratio is drastically increasing, reaching an average value of 37 for the 31-45 µm grain size fraction. Note that standard deviations considering all analyzed layers for each grain size bin (represented by the error bars in Fig. 8) are decreasing from coarse-grained to fine-grained fractions, which suggests that component proportion variability from a layer to another is decreasing towards fine-grained fractions. Note that no distinctive quantification has been made between the different juvenile components (complexity of the observed textures would often lead to significant and unquantifiable errors). However, preliminary observations made through different grain size fractions and layers, suggest that juvenile pumice and dense glassy are dominant compared to the juvenile scoria within the coarse-grained (lapilli and coarse ash) and fine-grained (fine ash) fractions respectively. Juvenile scoria grains are almost absent in the fine-grained fractions (Fig. 7).

As shown by ash morphology measurements, all 2005 analyzed layers (KAR_10_a, b, c, j, k, l, n and o) show similar morphological signatures and ranges, looking at similar grain size fractions (Table S3). However, focusing on a representative layer of both 2005 paroxysms (KAR_10_a), ash morphology quantifications (Table S3) show differences in function of the observed grain sizes: SLD (Fig. 9a), CVX (Fig. 9b) and SPH (Fig. 9c) ranges progressively evolve toward higher values with decreasing grain sizes, reflecting the occurrence of relatively irregular-shaped and/or smoothed particles within coarse grain size fractions (e.g., 500-1000 µm), whereas blocky-shaped and/or angular particles dominate within finer grain size fractions (e.g., 63-125 µm). AR parameter exhibits the higher ranges of values (Fig. 9d) for deposits from the 1977 eruption (KAR_1977_a) and both 2005 paroxysms. This variability does not change with grain size and reflects that elongated or blocky

485 equidimensional grains coexist within the deposits. On the whole, 2005 ash particles have a
486 significantly different morphological signature than to those of the 1977 eruption (Fig. 9). This shift
487 reflects the presence of both well rounded and highly elongated particles within the 1977 magmatic
488 sample, leading to a wider range of fluidal morphologies in terms of SLD, CVX, SPH and AR, compared
489 2005 samples. Note that the significant data overlap between the 1977 and 2005 samples is
490 reinforced by the occurrence of abundant olivine loose crystals within the crystal-rich 1977 sample,
491 which have similar morphological properties as the blocky-shapes and angular 2005 particles.

492 **4.3. Textural quantifications on porosity**

493 VSD analysis performed on the coarse juvenile ash particles (700-1000 μm) shows distinct
494 results for the pumice grains (Fig. 10a) and for the scoria grains of the April and November 2005
495 paroxysmal deposits (Fig. 10b). VSDs of pumice grains show, on average, a symmetrical and unimodal
496 distribution, vesicle diameters ranging from 5 to 400 μm with a main mode around 90 μm. Note that
497 KAR_1_c and KAR_1_n samples have a second but minor VSD mode between 200 and 400 μm. On all
498 these pumice grains, the measured vesicle content is 61 vol% on average. In contrast, VSDs of scoria
499 grains show, on average, a significantly different distribution, vesicle diameters still ranging from 5 to
500 400 μm but with an asymmetrical distribution, main modes being shifted towards larger vesicle
501 diameters (between 100 and 200 μm) and with second minor modes up to 400 μm. Moreover, the
502 measured vesicle content is half (31 vol%) that of the pumice grains. The 1977 ash show a slightly
503 different pattern from the two 2005 components described before (Fig. 10b): a unimodal distribution
504 is observed, with vesicle diameters ranging from 10 to 400 μm and with a mode at around 120 μm
505 and a total vesicle content of 54 vol%.

506 Textural distinctions between these different components are also visible focusing on N_V and
507 V_G/V_L values (Fig. 10c). N_V values for both pumice and scoria grains range in the same order of
508 magnitude (from 2 10^4 and 8 10^4 mm^{-3}) and have similar average values (4.5 10^4 and 4.7 10^4 mm^{-3} for
509 pumice and scoria respectively). On the other hand, V_G/V_L ratios are significantly lower in the scoria
510 than in the pumice grains (1.46 and 0.53 respectively). Note that the 1977 sample show the lowest
511 N_V (2.4 10^4 mm^{-3}) with an intermediate V_G/V_L ratio (1.17).

512 Finally, porosity and vesicle connectivity measurements (Fig. 10d) highlight that the juvenile
513 lapilli fragments (both pumice and scoria clasts) from both 2005 eruptions have relatively high
514 porosities (from 61 to 90 vol%, 82 vol% on average) compared to the juvenile lapilli fragments from
515 the 1977 lava fountaining eruption (from 45 to 72 vol%, 60 vol% on average). In parallel, the
516 connected porosity measured within the 2005 lapilli clasts (from 71 to 95 vol%, 84 vol% on average)

517 are slightly lower than that measured on the 1977 lapilli clasts (from 66 to 99 vol%, 91 vol% on
518 average).

519 All the detailed data described in this section can be found on Table S4.

520 **4.4. Magma chemical composition evolution from 1977 to 2007**

521 Magma compositions, from the 1977 eruption until the 2007 one, show a complex
522 evolutionary trend (Fig. 11). The 1977 bulk rock composition shows a relatively high MgO content of
523 13.7 wt%, reflecting the olivine-rich nature of the emitted magma, with also a relatively high
524 CaO/Al_2O_3 ratio of 0.90 reflecting the presence of clinopyroxene (in accordance with the XRD
525 measurements and the optical observations). The next emitted magmas were aphyric, with, in April
526 2005, the lowest MgO content (6.4 wt%) and the lowest CaO/Al_2O_3 ratio (0.79) recorded on the 1977-
527 2007 period. Then, the November 2005 (6.6 wt% of MgO, CaO/Al_2O_3 ratio of 0.81), May-June 2006
528 (6.6 wt% of MgO, CaO/Al_2O_3 ratio of 0.81) and January 2007 (6.7 wt% of MgO, CaO/Al_2O_3 ratio of
529 0.83) magmas progressively show a slight increase in these values.

530 Matrix glass compositions (Fig. 11) show similar or lower MgO and CaO/Al_2O_3 ratio values
531 from each corresponding bulk rock composition. Glass compositions closed to bulk rocks correspond
532 to uncrystallized pumiceous and dense glassy grains, while glass compositions that are progressively
533 depleted in MgO content with decreasing CaO/Al2O3 ratios correspond to partially crystallized scoria
534 grains.

535 Crystals of plagioclase, clinopyroxene and olivine, as well as Fe-Ti oxides were analyzed for
536 the 2005, 2006 and 2007 eruptions. Only one euhedral micro-phenocryst of plagioclase was
537 measured at An_{78} (November-December 2005 eruption, in equilibrium with the bulk rock
538 composition) whereas 27 microlites (dendritic texture in scoria grains) of plagioclase were measured
539 ranging from An_{55} to An_{66} for the 2005 and 2007 eruptions (in equilibrium with their surrounding
540 depleted matrices). 46 clinopyroxenes were analyzed, for the 2005, 2006 and 2007 eruptions,
541 showing compositions ranging between salite and augite. 60 analyses were realized on olivine
542 crystals for the 2005, 2006 and 2007 eruptions, ranging from Fo_{39} to Fo_{86}: Fo_{81-86} olivines are euhedral
543 antecrysts that were measured in the May-June 2006 products, Fo_{76-81} olivines are euhedral or
544 skeletal micro-phenocrysts that were measured in the 2005, 2006 and 2007 eruptions and in
545 equilibrium with their corresponding bulk rock compositions, and Fo_{39-76} olivines are dendritic
546 microlites in equilibrium with their surrounding depleted matrices that were mainly analyzed in the
547 2005 scoria products.

All the detailed data described in this section, as well as crystal compositions and REE concentrations can be found on Table S5.

5. Discussion

The distinction between magmatic and phreatomagmatic fragmentation regimes, especially concerning mafic magmas, is widely discussed in volcanology (e.g., Houghton et al., 1996; Ort and Carrasco-Núñez, 2009; Graettinger et al., 2013; Colombier et al. 2019a, Latutrie and Ross, 2020; Thivet et al., 2020c), but in some cases, is unattainable looking only at deposit features of a given eruptive event (White and Valentine, 2016). In our study, pre-, syn and post-eruptive visual observations of the active crater are available, providing a reliable support for interpreting on the eruption dynamics (Fig. 2). We also had the opportunity to study a complete and well-preserved deposit sequence (Fig. 3), representative of the two targeted explosive events. In this section, both magmatic and phreatomagmatic processes are addressed in order to explain the physical characteristics of the related deposits and products, such as grain size (Fig. 3), texture (Figs. 4, 5, 6, 7 and 10) and shape variations (Fig. 9), as well as grain components distributions (Fig. 8) and chemical compositions (Fig. 11).

5.1. The magmatic contribution on the conduit conditions: magma degassing and ascent rates controlling the initial eruptive dynamics

Pre-eruptive seismic activity recorded since mid-2003 suggested a deep magmatic input from 20 km below sea level under the summit caldera (Bachèlery et al., 2016). Deep volcano-tectonic events were recorded both before and during the 2005 eruptive events by the seismic network of the Karthala Volcano Observatory (OVK). This seismic unrest anticipated a new phase of intense eruptive activity, the highest since the phreatic eruption of 1991 and heralded the 2005-2007 sequence of eruptions (Bachèlery et al., 2016). The decrease of both CaO/Al_2O_3 ratio and MgO content starting from April 1977 (composition corrected for the cumulative olivine content, step 1 in Fig. 11) to April 2005 bulk rocks (step 2 in Fig. 11), reflects a differentiation trend within feeding magmatic system during this period. We can speculate that volatiles concentration increased in the cooling and evolved melts during the 1977-2005 time period. On the other hand, the progressive increase of MgO and CaO/Al_2O_3 values from April 2005 and January 2007 eruptions reflects progressively less evolved compositions during this period and highlights that a new magma input is progressively contributing to the April 2005, November-December 2005, May-June 2006 and January 2007 eruptions (step 3 in Fig. 11). The eruption of these magmas is likely the result of the mixing of this evolved and this more primitive magmatic components.

581 **5.1.1. Insights from the juvenile pumice component**

582 Because of their small size and their textural signatures suggesting their interaction with
583 external water, we are confident that the analyzed ash particles are rapidly quenched when formed
584 (Xu and Zhang, 2002), hence representative of the magma texture and composition at the
585 fragmentation level.

586 The juvenile pumice component (Fig. 4), which is predominant within the 2005 fallout
587 deposits (Fig. 8), represents microlite-free and highly porous magma portions. Pumice ash grains are
588 characterized by high N_V values and high V_G/V_L ratios (Fig 10c), compared for instance to the recent
589 and typically weakly explosive basaltic eruptions of Piton de la Fournaise volcano (Thivet et al.,
590 2020a; 2020b). These data, together with mainly unimodal VSDs (Fig. 10a), suggest that the
591 corresponding magma portion exhibit one significant episode of degassing, resulting in bubble
592 nucleation and growth, during the relatively high magma decompression in the volcanic conduit
593 (Shea et al., 2010, 2017). From these insights, we can speculate the occurrence of a closed-degassing
594 regime for the magmas emitted during both paroxysms (Figs. 12a and 12b).

595 Pre-eruptive magma temperatures are estimated using the MgO-dependent thermometer
596 for basaltic melts (using bulk rocks) at atmospheric pressure, from Thivet et al. (2020a): 1121 and
597 1131 °C are the average estimated magma temperatures for the April and November-December
598 eruptions, respectively. In parallel, Lange et al. (2009) model, based on plagioclase-melt equilibrium,
599 is used to estimate residual dissolved H_2O content in the magmatic melts, giving relatively low
600 dissolved H_2O contents, typically < 1 wt%, for both eruptions. These estimations together with the
601 textural N_V parameter, are also used to quantify magma decompression rates using the N_V-
602 dependent decompression rate meter of Toramaru (2006). Relatively high N_V values measured within
603 several distinct deposit layers of both 2005 paroxysms lead to variable but relatively high magma
604 decompression rates between 0.16 and 0.31 MPa s^{-1} compared to relatively lower magma
605 decompression rates (< 0.15 MPa s^{-1}) estimated for recent and typically weak explosive basaltic
606 eruptions of Piton de la Fournaise (Thivet et al., 2020a, 2020b). Magma decompression rates are
607 typically linked with ascent and mass discharge rates (Gonnermann and Manga, 2003) as well as
608 eruptive dynamic regimes and fragmentation efficiencies (Cashman and Scheu, 2015). Interestingly,
609 the higher calculated decompression rate is from the KAR_2005b layer (0.31 MPa s^{-1}, corresponding
610 to an ascent rate of about 10 m s^{-1}), which corresponds to the last identifiable deposits of the
611 November 2005 paroxysm, which is also the coarsest tephra layer of the 2005 paroxysms sequence
612 (Fig. 3c). We suggest that this high decompression and ascent rate was the main contributor to the
613 formation of a short-lived but intense lava fountaining at the origin of the deposition of the

KAR_2005b layer that is part of a relatively large bomb field area (Fig. S1c). Vesicle connectivity measurements performed on lapilli clasts fit with this interpretation as these measurements fall in the range characterized by sustained lava fountaining (Fig. 10d). As a comparison, the measured clasts from the 1977 eruption show relatively lower porosities and lower vesicle connectivity values, reflecting much less intense magmatic activities ranging between Hawaiian-style and mild Strombolian-style dynamics. The absence of fine ash particles in the KAR_2005b layer (Fig. 3c) suggests the predominance of purely magmatic dynamics that can be explained by the progressive end of phreatomagmatic dynamics as the intra-crateric water lake and the water table system dried up. The short-term increase in magma ascent rate may also have contributed to the cessation of water-magma interactions (Fig. 12b). Note that non-juvenile blocks and coarse ash present in the KAR_2005b layer are either attributed to remnant steam explosions or to purely magmatic processes that can produce such deposits, as supposed for instance at Stromboli (Métrich et al. 2005; Calvari et al. 2006).

5.1.2. Insights from the juvenile scoria component

Besides the juvenile pumice component, variably crystallized magmatic portions are associated with the presence of the juvenile scoria component (Fig. 5), which occurred in all the studied layers but in relatively small proportions (as also shown in Carlier, 2019). We associate this scoria component with a process of crystallization near the conduit margins, induced by degassing during the magma decompression that is a common process in basaltic melts (e.g., Lipman et al., 1985; Applegarth et al., 2013; Thivet et al., 2020b). More than a crystallization process, it can be referred as a zoning of the textural features of the ascending magma column (Fig. 12). The occurrence of syn-eruptive crystallization during both 2005 Karthala paroxysms, and also during the 2006 and 2007 relatively weak explosive eruptions, is evidenced by differentiated glass compositions (microlites of olivine deplete the MgO content of the glass and microlites of clinopyroxene and plagioclase decrease or increase the CaO/Al_2O_3 ratio, respectively) with respect to their bulk rock counterparts (step 4 in Fig. 11). Crystal compositions and textures can also be used as an indicator of the presence of this degassed magma: degassing-driven crystallization usually forms dendritic textures with no preferential orientations and most likely occurred during the final stages of the magma ascent before the fragmentation (Applegarth et al. 2013). This explains why the analyzed microlites are not in equilibrium with the bulk rocks but rather with their surrounding depleted matrices.

The occurrence of microlites in the scoria component is also associated with vesicle coalescence and gas loss processes, clearly visible on VSDs and N_V vs. V_G/V_L patterns (Figs. 10b and

10c). This textural evolution reflects that a large proportion of the magma in the conduit is bubbly and non-crystallized (corresponding the juvenile pumice component) while small proportion is more degassed and crystallized (corresponding to the juvenile scoria component). This leads to a drastic increase in magma viscosity from 10^2 (juvenile pumice) to 10^9 Pa s (fully crystallized scoria portions) using the three-phase viscosity model, which integrates Maron and Pierce (1956), Llewellin and Manga (2005), Giordano et al. (2008), Mader et al. (2013) and Truby et al. (2015) models. In some cases, this increase of magma viscosity can drastically change eruptive dynamics and increase the magma fragmentation efficiency (e.g., Sable et al., 2006, 2009; Thivet et al., 2020a, 2020c). However, the viscous portion identified in all analyzed layers from both 2005 Karthala paroxysms, was not dominant enough, especially within the fine tephra fractions, to be considered as the main process leading to increasing fragmentation. Moreover, the occurrence of differentiated melts within the 2006 and 2007 weak explosive eruptions (Fig. 11), with a composition close to that of the scoria components, confirm that this syn-eruptive crystallization process cannot be at the origin of the main fragmentation mechanism observed during the 2005 paroxysmal phases.

5.2. The phreatomagmatic contribution on the fragmentation efficiencies: water-magma interactions controlling the formation of a wide range of tephra in terms of component and size

5.2.1. Insights from the non-juvenile component

The occurrence of non-juvenile particles within the 2005 paroxysmal deposits (Fig. 6) is interpreted as a typical consequence of water-magma interactions (e.g., Self et al., 1980; Dvorak, 1992; Dzurisin et al., 1995; Houghton et al., 1996; Doubik and Hill, 1999). The presence of large (up to meters) blocks of old and dense lavas within proximal fallout areas (Figs. 2e, S1c and S3c), suggests the occurrence of thermohydraulic explosions (Thiéry and Mercury, 2009; Montanaro et al., 2021) and associated shock waves (Büttner et al., 2005) able to fragment and project these ballistics (Fig. 12), originating from dense, crystallized and sometimes oxidized lava and micro-gabbro units that are visible on the crater walls (Fig. 2). The absence of extended hydrothermal alteration on these non-juvenile particles suggests that they are fragmented within the upper 1 km of the volcano (corresponding to the thick water-satured rock unit), as the hydrothermal system is located deeper and represent a weak activity in the Choungou-Chahalé crater area (Lénat et al., 1998; Savin et al., 2001, 2005; Bernabeu et al., 2018; Liuzzo et al., 2021).

Within medial and distal fallout areas, block occurrence rapidly decreases (Fig. S1c) as they travelled in ballistic paths. In parallel, non-juvenile particles are mainly observed within relatively coarse grain size fractions of fallout deposits (Fig. 8). This distribution pattern suggests that

679 phreatomagmatic-induced host rock fragmentation mainly contributes to the formation of coarse
680 tephra grains but do not contributes to the significant formation of fine ash particles.

681 **5.2.2. Insights from the juvenile dense glassy component**

682 Active or interactive particles are tephra grains that exhibit Molten Fuel-Coolant Interactions
683 (MFCIs), which in the case of phreatomagmatic eruptions, are related to the interaction between
684 magmatic melts and external fluids, especially water (e.g., Büttner et al., 1999; 2002; Fitch and
685 Fagents, 2020). As shown by natural and experimental particles (Dürig et al., 2012a), they are
686 typically characterized by visible branching quench cracks and stepped features on their surface as
687 well as blocky shapes, reflecting the occurrence of crack bifurcation and shock wave propagations
688 induced by MFCIs and a dominant brittle fragmentation mechanism (Wohletz et al., 2013).

689 Within the 2005 paroxysmal deposits, these active particles (with stepped features and
690 cracks) mainly occur in the fine-grained juvenile dense glassy component (Fig. 7), suggesting that
691 brittle fragmentation induced by phreatomagmatism is the main contributor of the formation of fine
692 ash particles, which are not considerably formed during purely magmatic and weak explosive
693 activities (e.g., Parfitt, 1998; Thivet et al., 2020a; 2020c). Note that stepped features are not to be
694 confused with the ubiquitous hackle lines, which are not a direct diagnostic of phreatomagmatism
695 but only of brittle facture of glass. Nevertheless, many examples of interactive grains in the literature
696 include both stepped features and hackle lines (e.g., Heiken and Wohletz, 1987; Buttner et al. 1999;
697 Austin-Erickson et al., 2008).

698 The relatively high porosity of the initial magma, as shown by the coarse pumice fragments
699 (Fig. 4), also facilitated the fragmentation during the water-magma interactions, as relatively low
700 deformation energy is required to break highly vesicular material (Zhang 1999; Zimanowski et al.,
701 2015). This efficient brittle fragmentation led to the emission of fine dense ash fragments, made of
702 glassy vesicle wall fragments or glassy rinds (Mastin, 2007), which are inherited from the
703 fragmentation of the initial vesicular magma. The genetic link made between the coarse-grained
704 pumice and fine-grained dense glassy particles is also supported by the VSDs measured on coarse ash
705 particles, which show that the main porosity is represented by vesicles larger than 50 µm in diameter
706 (Fig. 10a), thus the main porosity cannot be recorded in particles finer than this size (Fig. 7). This
707 highlights the role of bubbles (and associated characteristics, especially high N_v) in generating fine
708 ash during hydromagmatic eruptions (Liu et al., 2015). The rapid stress and deformation processes,
709 as well as volatile degassing from the melt, occurred shortly before and at fragmentation (e.g.,
710 Dingwell, 1996; Papale, 1999, Dürig et al., 2012b). These fast processes probably caused a rapid
711 transition from a viscous regime (above the glass transition temperature) to a brittle regime (below

712 the glass transition temperature), whose textural footprints might be identifiable in some ash grains,
713 in which vesicle walls are highly deformed and/or broken (Figs. 4f and 4g), also suggesting the
714 occurrence of in situ particle granulation (Colombier et al., 2019a).

715 The fact that no significant variations were observed in ash morphology for the investigated
716 2005 layers and for a same grain size fraction (also shown in Carlier, 2019), suggests that similar
717 fragmentation mechanisms occurred during both 2005 paroxysms. The comparison made between a
718 1977 and a 2005 ash sample has been performed (Fig. 9) in order to focus on ash morphology
719 variations in function of the nature and origin of the deposits (weak magmatic vs. strong
720 phreatomagmatic activities respectively) as well as of the grain size fractions. The 1977 deposit,
721 contain smooth, rounded as well as Pele's hair and tear particles (Fig. 9) that are typically absent in
722 the 2005 ash deposits but present in other deposits associated with Hawaiian-like activities (e.g.,
723 Cannata et al., 2019; Thivet et al., 2020a; 2020c). Brittle and efficient fragmentation is better
724 recorded in the 2005 fine ash fraction, as solidity, convexity and sphericity shape parameters tend to
725 higher values, typically reflecting blocky shapes (Figs. 9a, 9b and 9c).

726 The occurrence of accretionary lapilli within the 2005 deposits (Fig. S5), gradually composed
727 of relatively coarse particles in their cores to relatively fine particles in their rims (Fig. 7b), support
728 the idea that these ash particles were produced by phreatomagmatism and transported within wet
729 plumes (Houghton et al., 2015), in which accretionary lapilli can develop from a wet nucleus thanks
730 to surface tension and electrostatic attraction (Colombier et al., 2019b).

731 **5.3. Insights from observational data and knowledge of the summit area of Karthala volcano**

732 Lénat et al. (1998) and Savin et al. (2001) highlight that the Choungou-Chahalé crater,
733 periodically hosting a water lake, is underlain by a maximum of 1 km of water-saturated rocks. Both
734 April and November-December 2005 eruptions, which began with paroxysmal phases producing high
735 ash-rich plumes, occurred when water lakes were visible at the bottom of the Choungou-Chahalé
736 crater. Water-magma interactions can thus have occurred both during dyke propagation through the
737 water-saturated rocks and at shallow level at the surface water lake. Each paroxysmal phase was
738 then followed by a lava pond and weak explosive (lava fountaining) activity, from the same vent area
739 feeding the paroxysmal activity and after the disappearance of the intra-crateric water lake. This
740 evolution highlights that the lakes were rapidly heated and vaporized in contact with the hot magma
741 rising to the surface during the initial paroxysmal phases. We can thus infer that the water/magma
742 ratio evolved from relatively high values at the beginning of the eruption and tended to zero over
743 time, within a short duration of around 24 hours for each 2005 paroxysm. These contrasting water-
744 magma interactions (Fig. 12) resulted in different degree of released energy for the magma/rock

745 fragmentation (e.g., Frazzetta et al., 1983; Sheridan and Wohletz, 1983; Wohletz and McQueen,
746 1984; Wohletz et al., 2013; Houghton et al., 2015; Zimanowski et al., 2015).

747 Also, lava emissions observed during both 2005 eruptions after the paroxysmal phases,
748 resulted in the elevation of the crater bottom, which caused the absence of visible water at the
749 surface after the November-December 2005 eruption. The notable absence of water lake before,
750 during and after the May-June 2006 eruption can thus be correlated with its effusive and weak
751 explosive behavior (Fig. 2d). Furthermore, these newly emitted lavas represent a new thermo-
752 lithological boundary within the crater floor, which can significantly drag hydrothermal fluids from
753 the crater center towards peripheral areas (Bernabeu et al., 2018). Interestingly, the northern
754 caldera lobe and the northern rift area hosts the strongest hydrothermal activity (fumaroles and soil
755 degassing) of the volcanic system (Liuzzo et al., 2021) and produce dominantly effusive activities
756 (e.g., 1965; 1972; 2007), whereas the hydrothermal activity is much weaker in the area of the central
757 Choungou-Chahalé crater that feeds the most violent explosive activity (e.g., 1918; 1991; 2005). This
758 geographical pattern suggests that, in the whole 2005-2007 Karthala activity, hydrothermal activity
759 did not contribute to modulate the degree of explosivity. On the other hand, we can infer that a link
760 exists between the occurrence of shallow water (i.e. the water lake and associated water-saturated
761 rocks) and the degree of explosivity.

762

763 **6. Conclusions**

764 Field observations and laboratory analyses performed on the 2005 eruptive deposits of
765 Karthala volcano permit to identify and quantify distinct eruptive processes.

766 1 – Initial syn-eruptive magmatic processes, especially degassing (dominance of highly porous
767 magma portions) and in a less important proportion crystallization (occurrence of microlite-rich
768 portions) within the volcanic conduits were relatively significant during the two 2005 paroxysmal
769 phases compared to the weak explosive basaltic eruptions forming lava fountains (i.e., 1977's
770 Karthala eruption). However, these processes alone could not lead to the observed characteristics of
771 the deposits (i.e., occurrence of non-juvenile block to coarse ash particles, as well as abundant
772 accretionary lapilli and fine ash particles).

773 2 – MFCI interactions between highly porous magmatic melts and external water occurred
774 during the initial paroxysmal phases, leading to brittle and efficient fragmentation mechanism and
775 forming a large amount of fine ash from the initial porous magma. Thermohydraulic explosions

caused by the water-magma interaction resulted in the host rock fragmentation, forming relatively coarse (from blocks to coarse ash) non-juvenile particles.

3 – Fluctuating host rock and magma fragmentation efficiencies can be controlled by the variability of water/magmatic melt ratios through the eruptions. In natural systems, access of the magma to water includes many parameters difficult to assess (e.g. variations of magma ascent rate, surface area to volume ratios, vent shape, host rock permeabilities, amount and variations of syn-eruptive debris within the eruptive vent, Houghton et al., 2015). This makes phreatomagmatic interactions more complex than theoretical and experimental models. However, in the present study we argued and conclude that the observed deposit variabilities in term of grain size, grain componentry and layer thickness might be linked by variable phreatomagmatic interactions, which released variable energy, resulting in variable fragmentation efficiencies. (i) Fine and unimodal (grain size modes < 90 µm) tephra layers (KAR_10_b, d, f, h, l, m, n, p, r, t and u) result from a relatively homogenous and efficient phreatomagmatic fragmentation (we can speculate relatively high water/magma ratios, Fig. 12a). This fragmentation regime can be short-lived or relatively steady as suggested by highly variable tephra layer thicknesses (from < 5 to 20 cm). (ii) Intermediate-sized and unimodal (grain size modes between 250 and 710 µm) tephra layers (KAR_10_a, j, k and q) result from homogeneous but relatively weak phreatomagmatic fragmentation mechanism (we can speculate intermediate water/magma ratios, Fig. 12a). (iii) Bimodal (the coarser modes being between 250 and 1400 µm and the finer modes being between 31 and 90 µm) tephra layers (KAR_10_c, e, g, i, o and s), originated from several combined mechanisms. The finest modes of these layers are mainly composed of juvenile material which undergone intense and efficient fragmentation. In contrast the coarser modes are composed of both inefficiently fragmented juvenile material (residual juvenile part of the phreatomagmatic fragmentation mechanism) and synchronously emitted non-juvenile coarse grains (from thermohydraulic explosions). (iv) The coarsest and unimodal (grain size mode between 5,66 and 8 mm) tephra layer (KAR_2005b), forming the uppermost part of the 2005 tephra sequence, mainly result from magmatic processes (Fig. 12b), forming a short-lived (tephra layer < 5 cm in thickness) but sustained lava fountaining episode at the end of the November 2005 paroxysm (which might be associated with remnant steam explosions forming non-juvenile blocks and coarse ash grains).

4 – Available external water volumes rapidly decreased during both 2005 paroxysms, which lasted only one day each, as the water vaporized and wet rocks dried in contact with relatively hot magmas and/or lavas and/or tephras. As the shallow system dried up, phreatomagmatic regimes progressively stopped for both 2005 eruptions, leading to lava pond and weak fountaining activities until the end of both 2005 eruptions.

In conclusion, and beyond field observations that were made at the time of the eruptions, the present study highlights the importance of in-depth analysis for such deposits in order to gain insights on shallow magmatic systems and associated processes potentially leading to relatively important and uncommon volcanic hazards.

Figures and tables

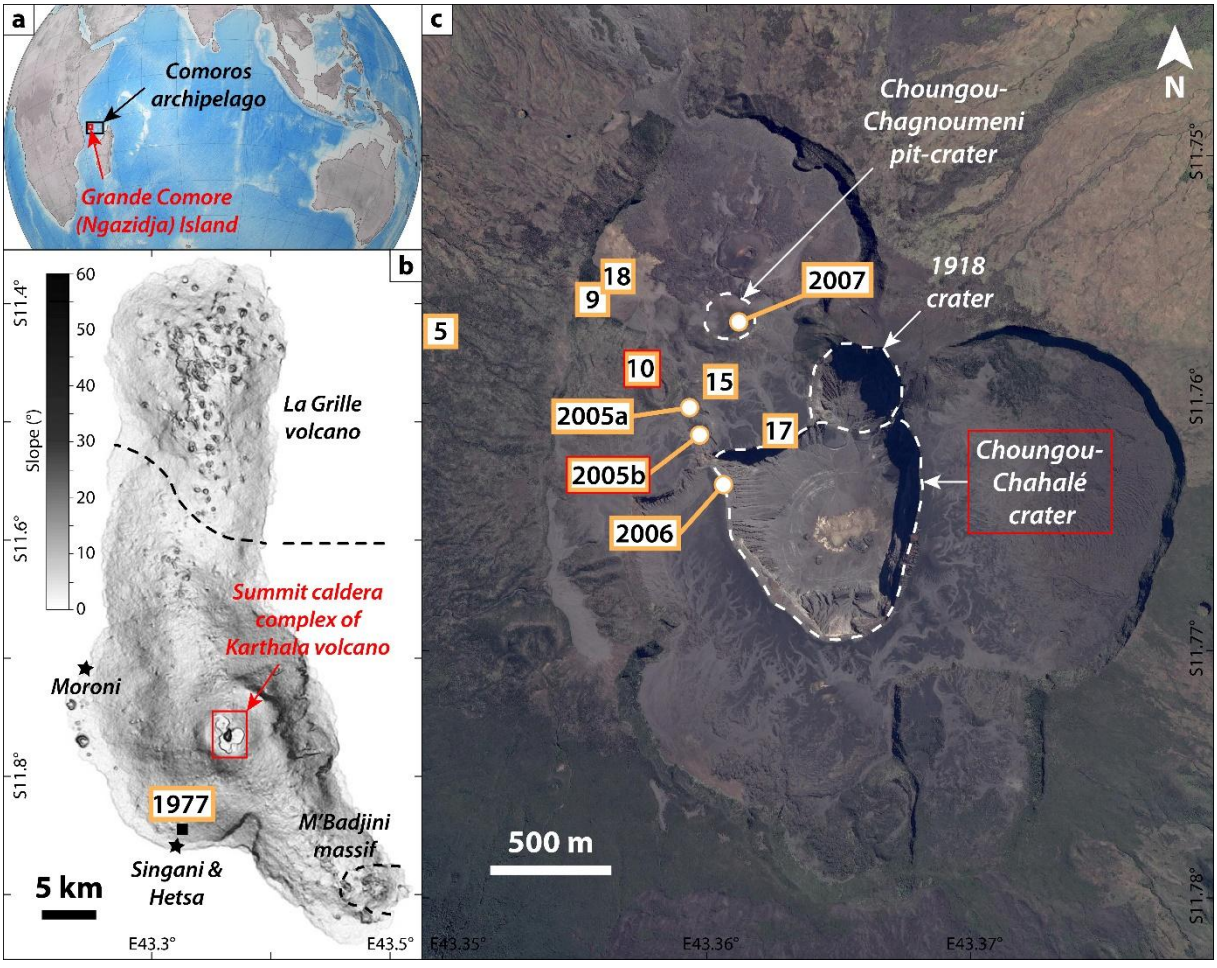

Figure 1 – (a) Location of the Comoros archipelago and the Grande Comore (Ngazidja) Island within the Mozambique Channel. (b) SRTM-derived slope map of the Grande Comore (Ngazidja) Island (modified from Bachèlery et al., 2016). The black square shows the location of the 1977 eccentric eruption and its associated sampling location (labelled 1977). Black stars show the capital city of Moroni and the adjacent villages of Singani and Hetsa. (c) Google Earth satellite image (CNES/Airbus, July 31, 2017) of the summit caldera complex of Karthala volcano. April 2005, November-December 2005 and May-June 2006 eruptive vents opened in the floor of the Choungou-Chahalé crater. The January 2007 eruption occurred in the Choungou-Chagnoumeni pit-crater. Numbered squares show the studied or sampling sites of both 2005 paroxysmal deposits (labelled 5, 9, 10, 15, 17, 18, 2005a and 2005b), as well as May-June 2006 (labelled 2006) and January 2007 (labelled 2007) eruptive products. Detailed location and description of each sample are shown in Table S1.

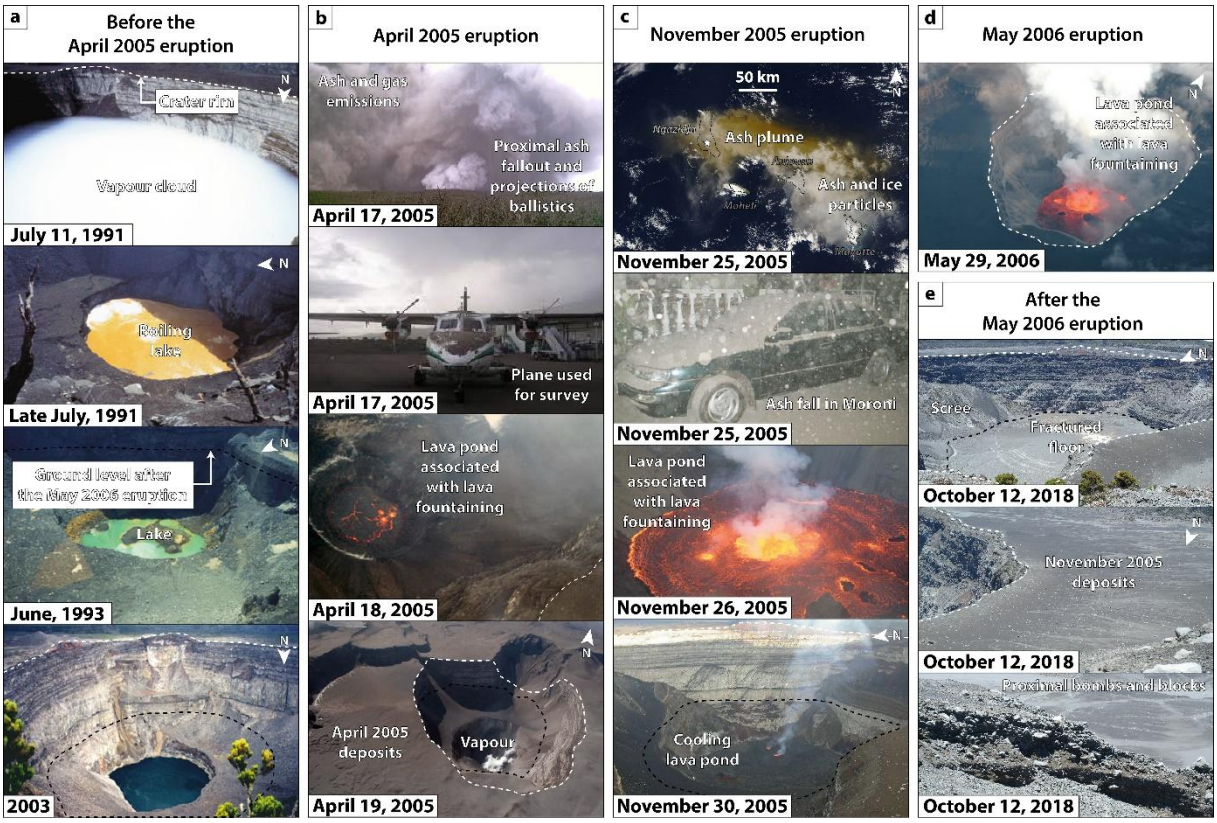

Figure 2 – Ground-, airplane- and satellite-based photographs showing the morphological evolution and eruptive activities that occurred within the Choungou-Chahalé crater, between 1991 and 2018. Dashed white lines show the Choungou-Chahalé crater rim and dashed black lines represent the

ground level of the Choungou-Chahalé crater floor after the May 2006 eruption. (a) Morphology of the Choungou-Chahalé crater and evolution of the water lake before the April 2005 eruption. Pictures taken by Patrick Bachèlery (modified from Bachèlery et al., 2016). (b) Chronology and impacts of the April 2005 eruption. From top to bottom, pictures taken by (i) Daniel Hoffschir, (ii) and (iii) Hamidi Soulé (modified from Bachèlery et al., 2016) and (iv) Nicolas Villeneuve. (c) Chronology and impacts of the November 2005 eruption. From top to bottom, (i) satellite image from NASA (Terra MODIS) white star representing the eruptive vent, (ii) pictures taken by Hamidi Soulé, (iii) Julie Morin (modified from Bachèlery et al., 2016) and (iv) François Sauvestre. (d) May-June 2006 eruption. Picture taken by Julie Morin (modified from Bachèlery et al., 2016). (e) Morphology of the Choungou-Chahalé crater after the May-June 2006 eruption. Pictures taken by Simon Thivet.

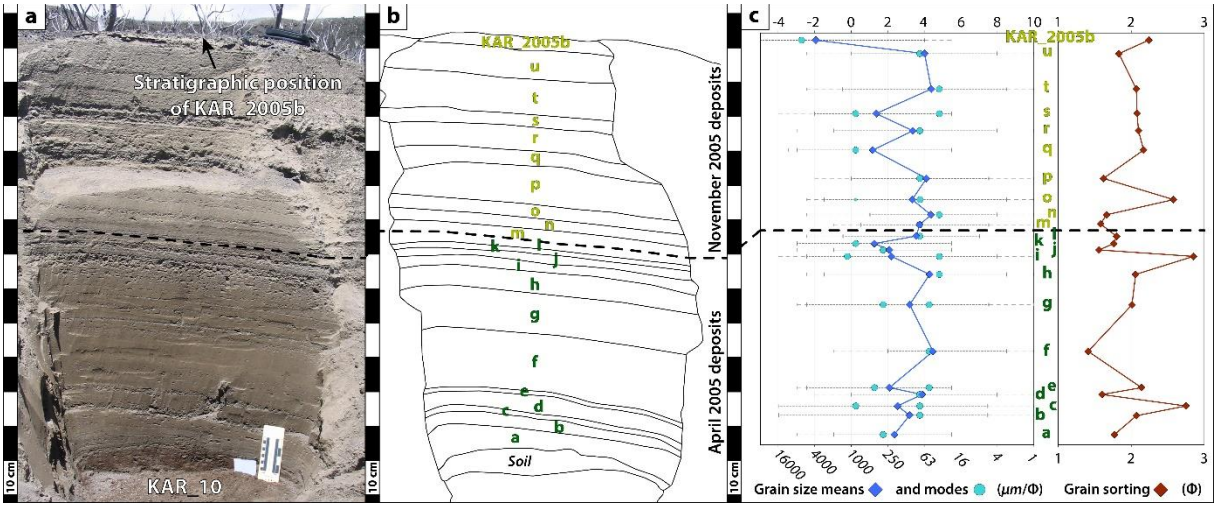

Figure 3 – (a) Picture of the KAR_10 stratigraphic log (cf. Fig. 1 for location), representative of the ash fallout deposits of both April and November 2005 paroxysmal phases. The thick dashed black line delimits the deposits from the two paroxysms. (b) Schematic of the same stratigraphic log with the different identified and sampled layers. Note that the very last products emitted by the November 2005 paroxysm are represented at the top of the log (KAR_2005b sample, cf. Fig. 1 for location). Layer names (from KAR_10_a to u, as well as KAR_2005b) are labelled in dark (April 2005) and light (November 2005) green. (c) Grain size mean, mode and sorting values of the sampled layers. Thin dashed lines represent the total grain size range of each sample and thick dashed lines only include

grain size fractions with > 1 wt% of the total mass of each sample. Detailed grain size analyses are shown in Table S2.

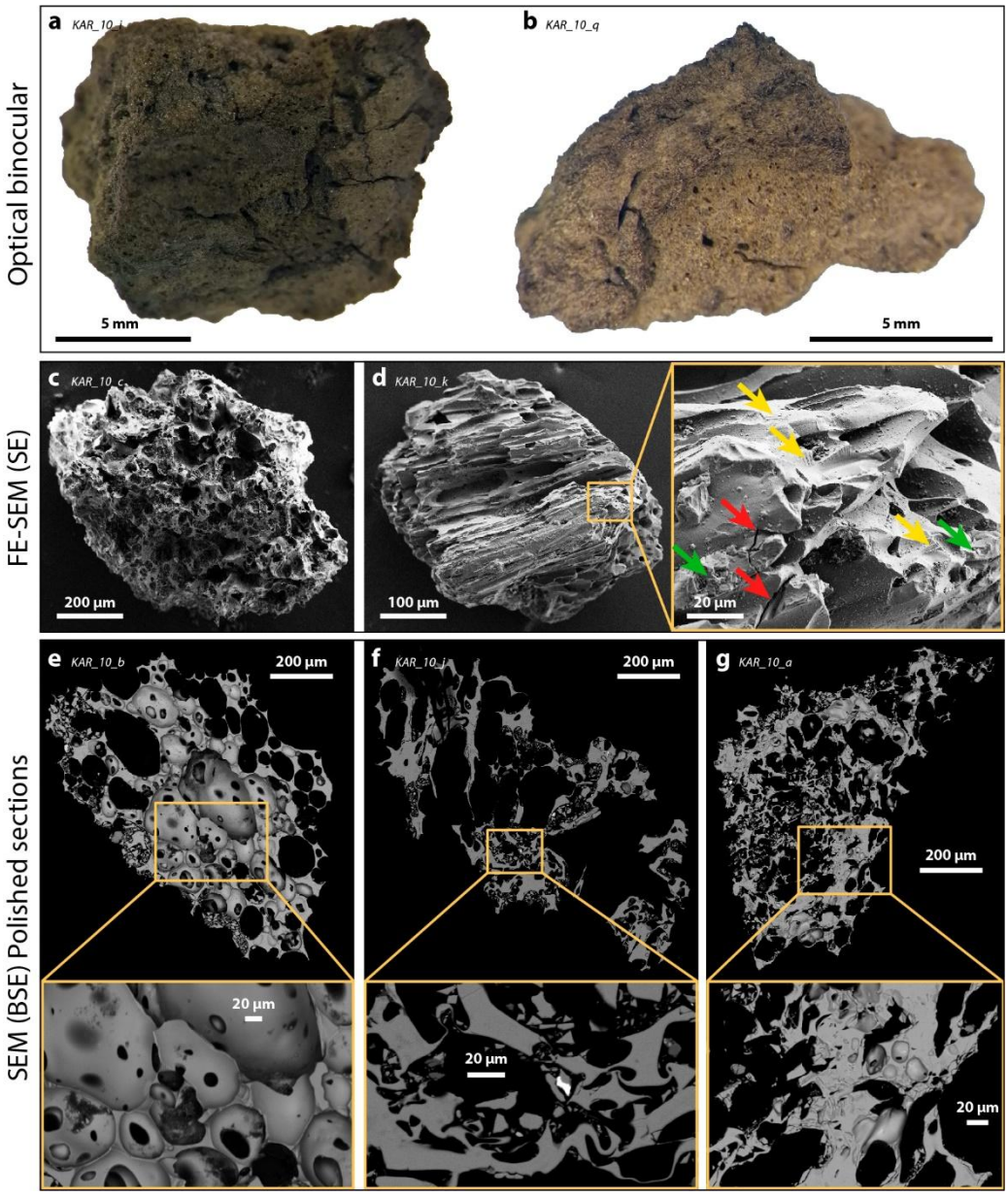

Figure 4 – Juvenile pumice clasts from both April and November 2005 paroxysmal fallout deposits. (a) and (b) Optical images of light brown lapilli fragments showing non-fluidal shapes and bread-crusted cracks on their surfaces. (c) and (d) 3D images of coarse ash (710-1000 µm) particles. Vesicles are either (c) rounded or (d) elongated. (d) Micron-scaled hackle lines (yellow arrows), stepped features (green arrows) and branching quench cracks (red arrows) are visible on the particle broken surfaces. (e), (f) and (g) Cross-section images of coarse ash (710-1000 µm) particles showing different deformation features from (e) rounded to (f) highly deformed and (g) broken vesicle walls.

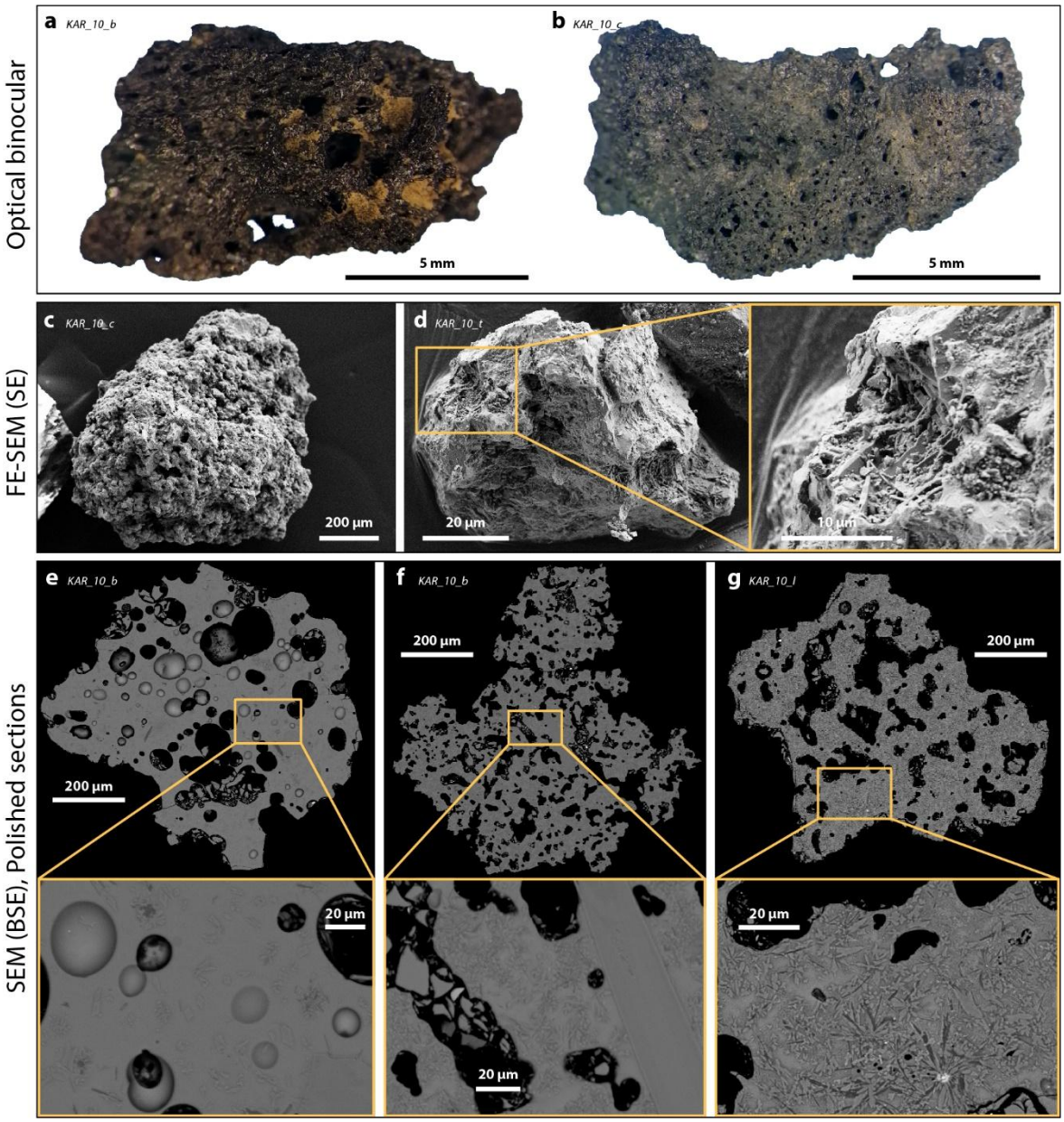

Figure 5 – Juvenile scoria clasts from both April and November 2005 paroxysmal fallout deposits. (a) and (b) Optical images of black lapilli fragments showing non-fluidal shapes. (c) and (d) 3D images of coarse ash (710-1000 µm) particles, characterized by rough or blocky surfaces. (d) Microlites are sometimes visible on their surface reflecting matrices with a high microlite contents. (e), (f) and (g) Cross-section images of coarse ash (710-1000 µm) particles showing a high range of crystallinity and porosity.

886

887

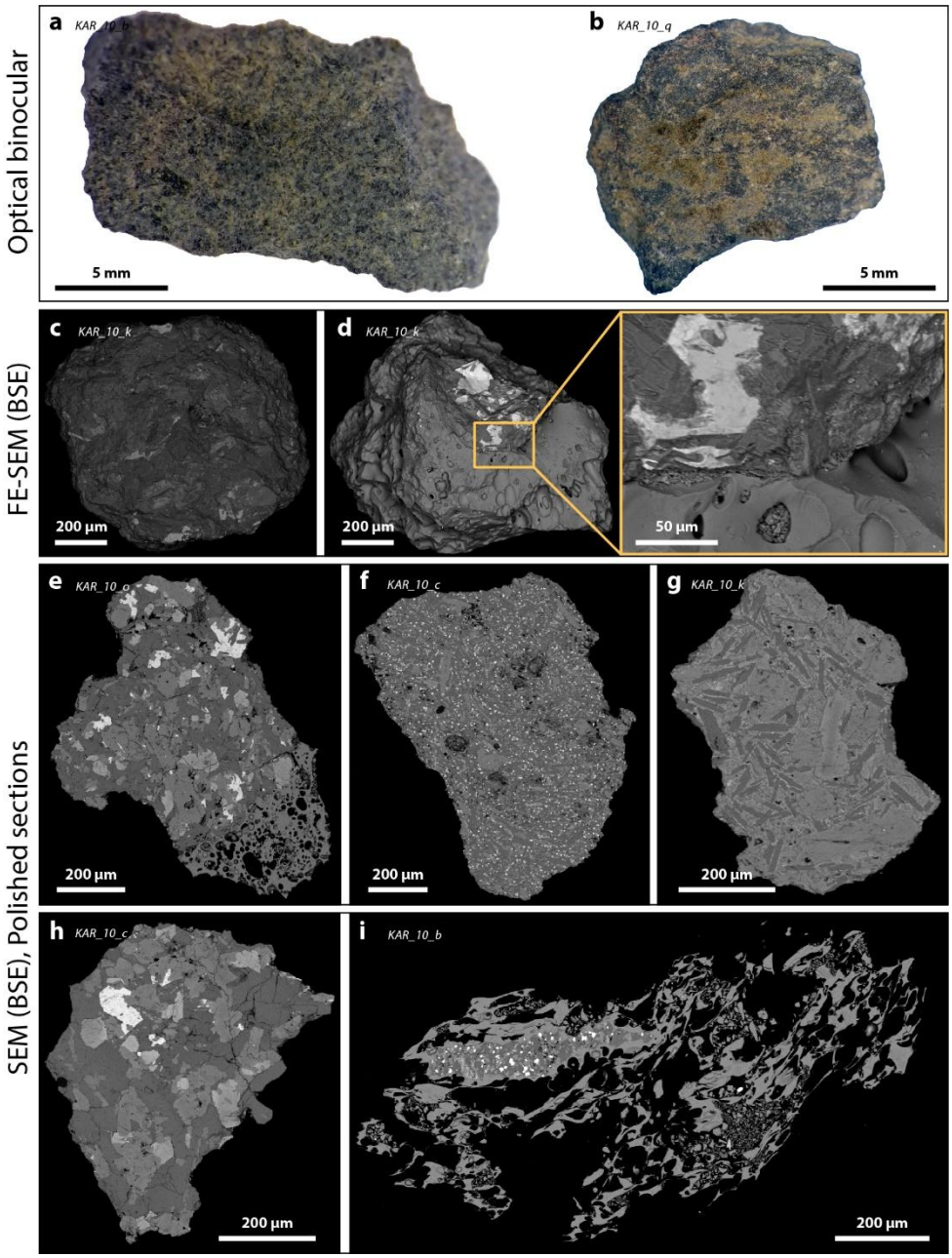

888

889 **Figure 6** – Non-juvenile clasts from both April and November 2005 paroxysmal fallout deposits. (a)
890 and (b) Optical images of dense lapilli fragments, with visible phenocrysts of plagioclase, pyroxene,
891 olivine and oxides. (c) and (d) 3D images of coarse (710-1000 µm) and dense micro-gabbroic ash
892 particles, characterized by blocky surfaces. (d) and (e) These non-juvenile fragments are sometimes
893 coated by the juvenile magma. (e), (f), (g) and (h) Cross-section images of coarse (710-1000 µm) ash
894 particles showing different textures in term of crystal size distribution, from tachylite-like to micro-
895 gabbro textures. Note the total absence of interstitial melts in these lithic fragments. (i) Cross-section

image of a micro-gabbroic fragment included within a juvenile pumice ash particle. In this case, this micro-gabbroic fragment is considered as juvenile as it is part of the erupted magma, and it also contains interstitial melt.

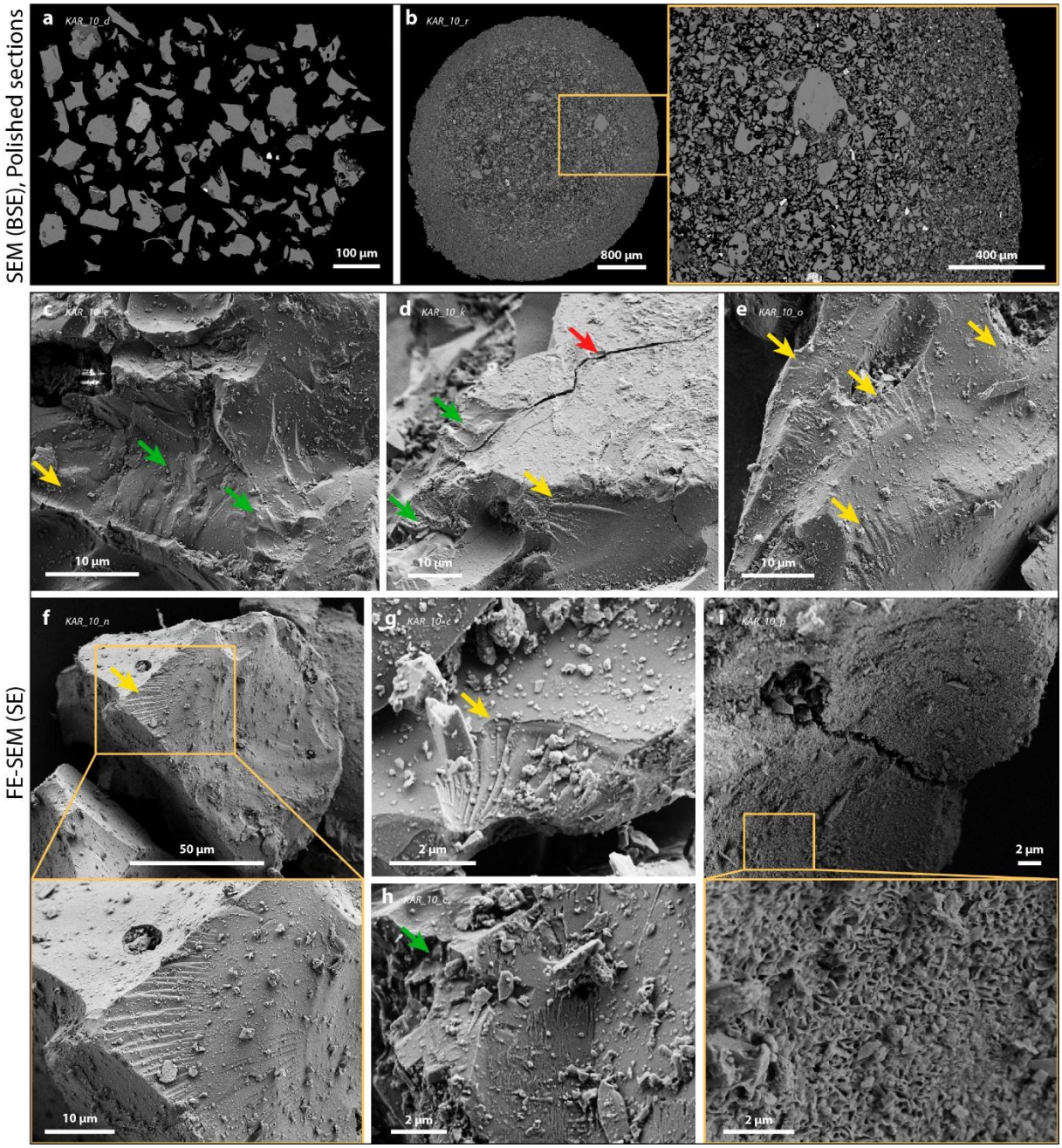

Figure 7 – Fine ash particles from both April and November 2005 paroxysmal fallout deposits. (a) Cross-section image of a sample showing the internal textures of the fine ash (< 63µm) particles. (b) Cross-section image of an accretionary lapilli. (c), (d), (e), (f), (g), (h) and (i) 3D images of fine ash (< 63 µm) particles. The fine-grained dense glassy particles show micron-scaled hackle lines (yellow arrows), stepped features (green arrows) and branching quench cracks (red arrows) on their surfaces. (h) and (i) Secondary deposition phases are also observed on some of the particle surfaces.

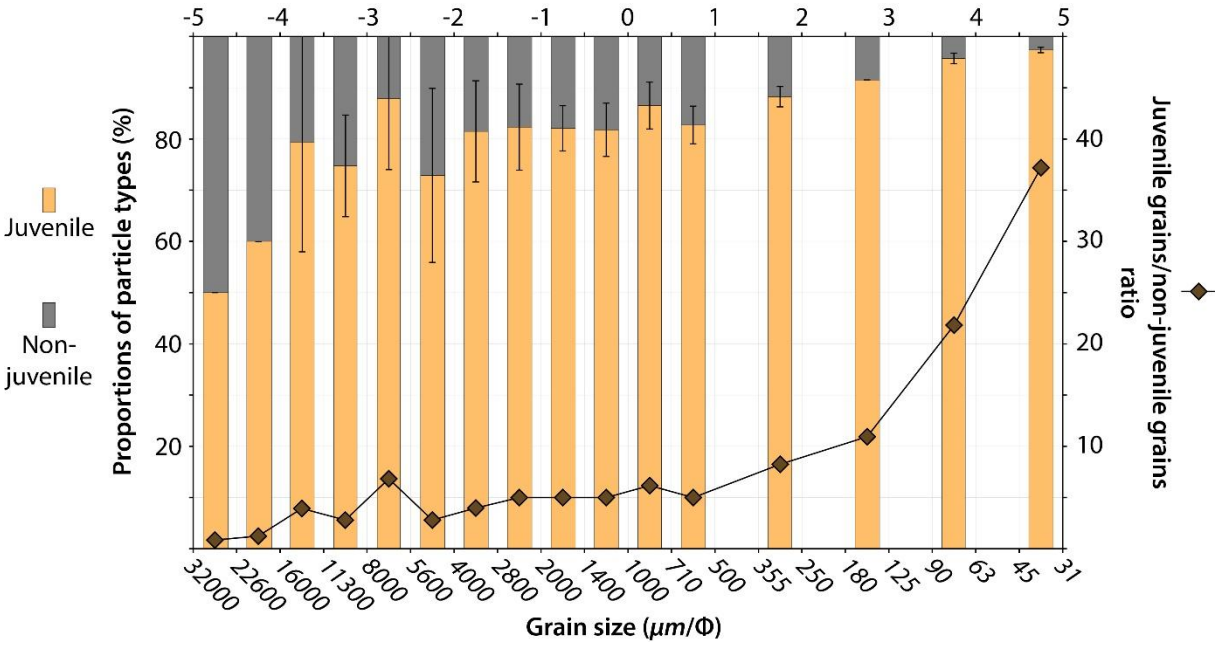

Figure 8 – Particle componentry analysis (juvenile vs. non-juvenile) of both April and November 2005 paroxysmal fallout deposits, in function of particle grain size. Each bar represents the average value (number %) for all the analyzed samples. Error bars represent the standard deviation to this averaged value, hence are representative of some local variations for some tephra layers. Detailed componentry analyses are shown in Table S3.

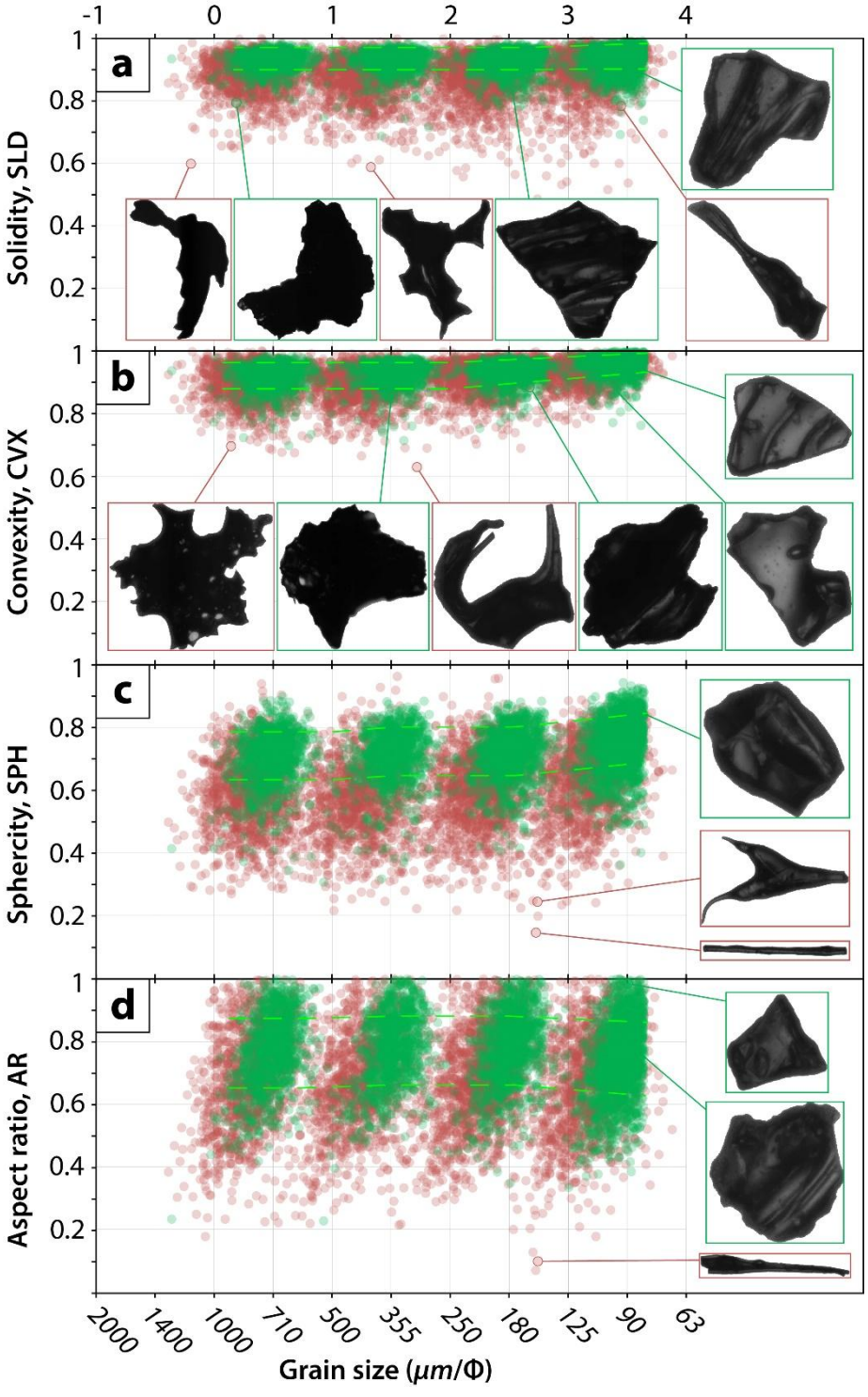

Figure 9 – Ash particle morphological analysis. (a) Solidity, (b) convexity, (c) sphericity and (d) aspect ratio values in function of particle grain size. Green dots represent the KAR_10_a sample from the April 2005 paroxysm, whereas the red dots represent the KAR_1977_a sample from the 1977

magmatic eruption that produced lava fountains. Green dashed lines represent the 2005 ash population within the standard deviation. Morphological raw data is presented in Table S3.

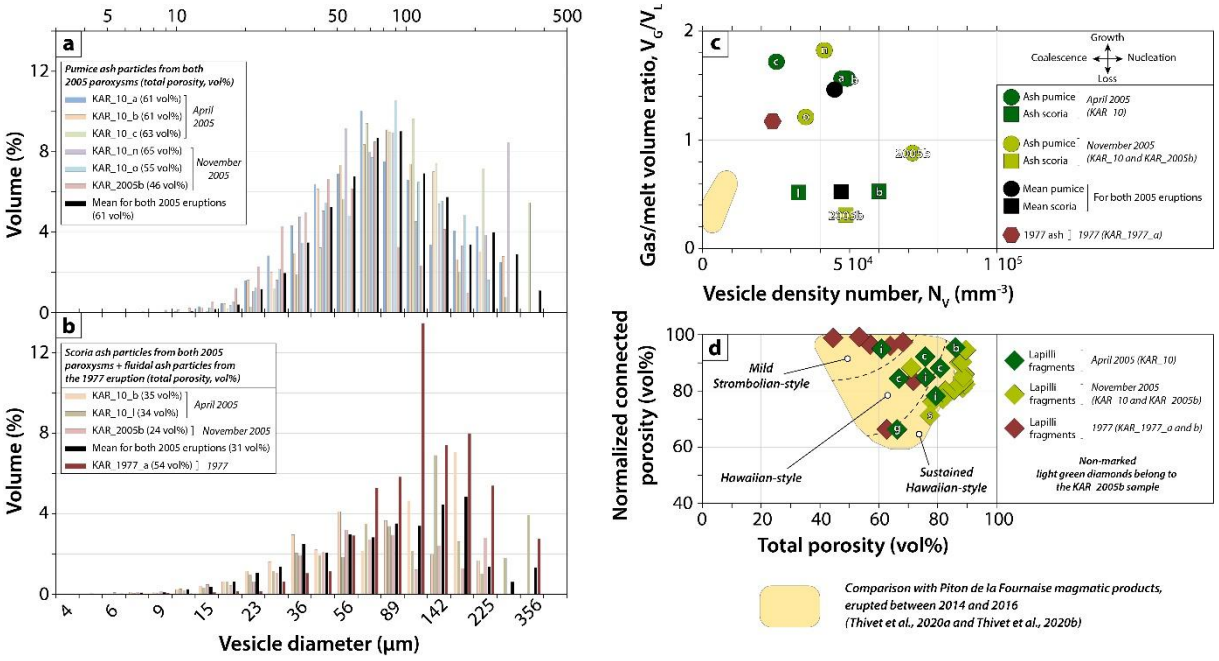

Figure 10 – (a), (b) and (c) Micro-texture and (d) bulk-texture analyses of both April and November fallout deposits as well as 1977 products. Vesicle size distributions of (a) pumice and (b) scoria (and 1977 lava fountains) ash particles. (c) Gas to melt ratios in function of vesicle density numbers for the same samples presented in (a) and (b). (d) Normalized connected porosity in function of total porosity for a selection of lapilli fragments from the 1977 eruption, as well as both April 2005 and November 2005 paroxysms. Detailed textural analyses are reported in Table S4.

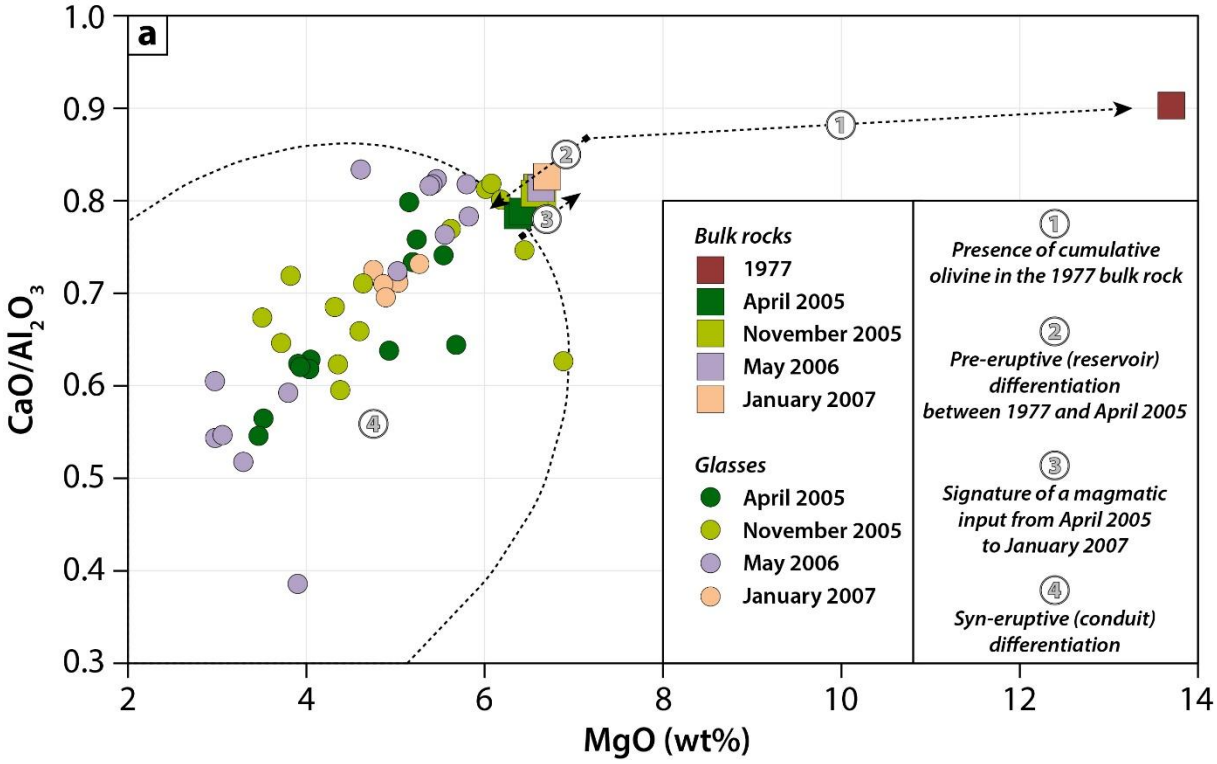

Figure 11 – (a) Bulk rock and glass compositions (CaO to Al_2O_3 ratio in function of MgO) of the magmas emitted between 1977 and 2007 at Karthala volcano, showing a complex magmatic evolution represented by the numbered steps. Error bars are included in the symbols.. Detailed bulk rock, glass and mineral analyses are reported in Table S5.

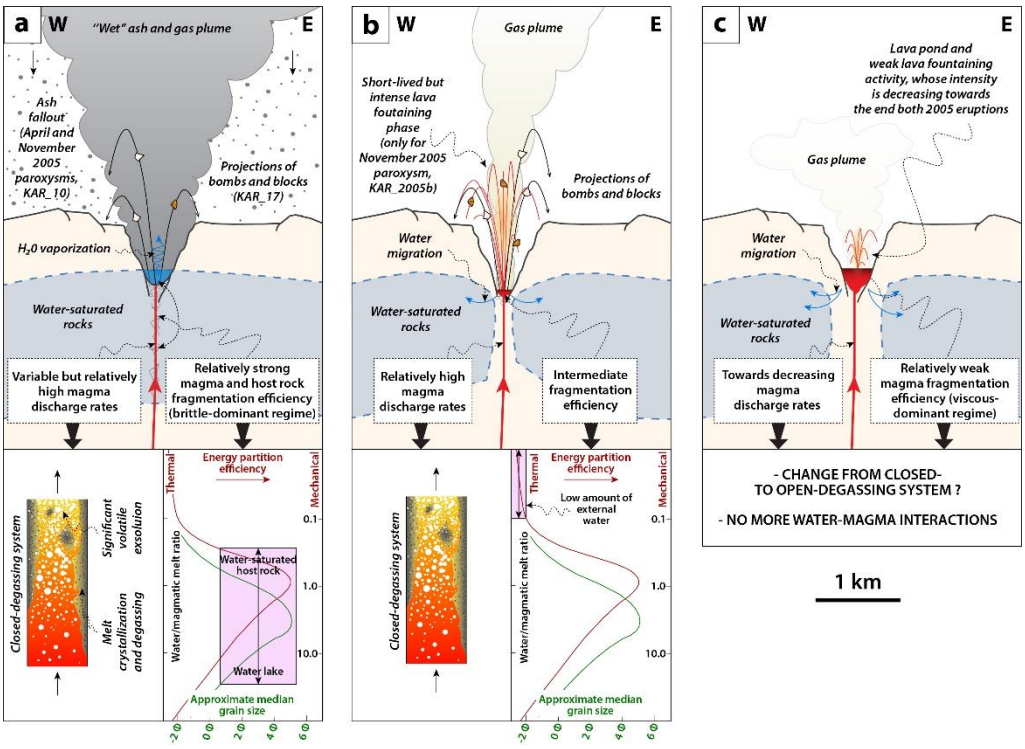

Figure 12 – Schematic sections of the shallow magmatic system of Karthala volcano, (a) during both 2005's paroxysms, (b) during the last phase of the November 2005 paroxysm and (c) during both 2005's lava pond activities. Shallow magmatic processes are represented on the bottom left hand side diagrams and water-magma interactions are illustrated in the bottom right hand side diagrams adapted from Wohletz et al. (2013).

Acknowledgments

We thank J-L. Devidal and E. Voyer for their invaluable help with the EPMA and SEM at the LMV and we thank A. Dalle for its help with the FE-SEM performed at 2MAtech. We are grateful to all members of the Observatoire Volcanologique du Karthala (OVK) for their support during the 2018 field work. We also thank the two reviewers for their highly constructive reviews. We acknowledge the support of the Interreg Hatari project. This research was funded by ClerVolc, the French Government Laboratory of Excellence initiative n°XXXX, the French government IDEX-ISITE initiative 16-IDEX-XXXX (CAP20-25), the Action Incitative of the Observatoire de Physique du Globe de Clermont-Ferrand (OPGC) and the Alexander Von Humboldt foundation.

983

984 **References**

985 Aiuppa, A., Burton, M., Caltabiano, T., Giudice, G., Guerrieri, S., Liuzzo, M., ... & Salerno, G. (2010).
986 Unusually large magmatic CO2 gas emissions prior to a basaltic paroxysm. Geophysical Research
987 Letters, 37(17). doi:10.1029/2010GL043837

988 Andronico, D., & Corsaro, R. A. (2011). Lava fountains during the episodic eruption of South–East
989 Crater (Mt. Etna), 2000: insights into magma-gas dynamics within the shallow volcano plumbing
990 system. Bulletin of volcanology, 73(9), 1165-1178. doi:10.1007/s00445-011-0467-y

991 Applegarth, L. J., Tuffen, H., James, M. R., & Pinkerton, H. (2013). Degassing-driven crystallisation in
992 basalts. Earth-Science Reviews, 116, 1-16. doi:10.1016/j.earscirev.2012.10.007

993 Austin-Erickson, A., Büttner, R., Dellino, P., Ort, M. H., Zimanowski, B. (2008). Phreatomagmatic
994 explosions of rhyolitic magma: Experimental and field evidence. Journal of Geophysical Research,
995 113(B11), B11201. doi:10.1029/2008jb005731

996 Bachèlery, P., Morin, J., Villeneuve, N., Soulé, H., Nassor, H., & Ali, A. R. (2016). Structure and
997 Eruptive History of Karthala Volcano. Active Volcanoes of the Southwest Indian Ocean. Active
998 Volcanoes of the World. Springer, Berlin, Heidelberg. doi: 10.1007/978-3-642-31395-0_22

999 Bachèlery, P., Hémond C. (2016). Geochemical and Petrological Aspects of Karthala Volcano. Active
1000 Volcanoes of the Southwest Indian Ocean. Active Volcanoes of the World. Springer, Berlin,
1001 Heidelberg. doi:10.1007/978-3-642-31395-0_23

1002 Bachèlery, P., Ali, D. B., Desgrolard, F., Toutain, J. P., & Coudray, J. (1995). L'éruption phréatique du
1003 Karthala (Grande Comore) en Juillet 1991. Comptes rendus de l'Académie des sciences. Série 2.
1004 Sciences de la terre et des planètes, 320(8), 691-698.

1005 Bachèlery P., Coudray J. (1993). Carte volcano-tectonique (1/50000e) de la Grande Comore et notice
1006 explicative. Edited by the French Embassy in Moroni, Comores, and The University of La Réunion, St.
1007 Denis de La Réunion

1008 Belousov, A., & Belousova, M. (2001). Eruptive Process, Effects and Deposits of the 1996 and the
1009 Ancient Basaltic Phreatomagmatic Eruptions in Karymskoye Lake, Kamchatka, Russia. Volcaniclastic
1010 Sedimentation in Lacustrine Settings, 35–60. doi:10.1002/9781444304251.ch3

1011 Bernabeu, N., Finizola, A., Smutek, C., Saramito, P., & Delcher, E. (2018). Spatio-temporal evolution of
1012 temperature and fluid flow through a new “thermo-lithological” boundary; the case of a pit crater of

1013 Karthala volcano (Comoros archipelago) refilled on January 13th 2007 by a lava flow. Journal of
1014 Volcanology and Geothermal Research. doi:10.1016/j.jvolgeores.2018.10.013

1015 Bonny, E., Thordarson, T., Wright, R., Höskuldsson, A. & Jónsdóttir, I. (2018). The Volume of Lava
1016 Erupted during the 2014 to 2015 Eruption at Holuhraun, Iceland: a Comparison between Satellite-
1017 and Ground-Based Measurements. Journal of Geophysical Research: Solid Earth,
1018 doi:10.1029/2017JB015008

1019 Büttner, R., Zimanowski, B., Mohrholz, C.-O., & Kümmel, R. (2005). Analysis of thermohydraulic
1020 explosion energetics. Journal of Applied Physics, 98(4), 043524. doi:10.1063/1.2033149

1021 Büttner, R., Dellino, P., La Volpe, L., Lorenz, V., & Zimanowski, B. (2002). Thermohydraulic explosions
1022 in phreatomagmatic eruptions as evidenced by the comparison between pyroclasts and products
1023 from Molten Fuel Coolant Interaction experiments. Journal of Geophysical Research: Solid Earth,
1024 107(B11), ECV-5. doi:10.1029/2001JB000511

1025 Büttner, R., Dellino, P., & Zimanowski, B. (1999). Identifying magma–water interaction from the
1026 surface features of ash particles. Nature, 401(6754), 688–690. doi:10.1038/44364

1027 Calvari, S., Spampinato, L., & Lodato, L. (2006). The 5 April 2003 vulcanian paroxysmal explosion at
1028 Stromboli volcano (Italy) from field observations and thermal data. Journal of Volcanology and
1029 Geothermal Research, 149(1-2), 160–175. doi:10.1016/j.jvolgeores.2005.06.006

1030 Cannata, C. B., De Rosa, R., Donato, P., Donato, S., Lanzafame, G., Mancini, L., & Houghton, B. F.
1031 (2019). First 3D imaging characterization of Pele's hair from Kilauea volcano (Hawaii). Scientific
1032 Reports, 9(1). doi:10.1038/s41598-018-37983-9

1033 Carlier, J. (2019). Insight into conduit dynamics and eruptive mechanisms of ash-forming basaltic
1034 eruptions: the case study of the 2005 eruptions at Karthala volcano (Grande Comore). MSc report,
1035 Université Clermont Auvergne, France, 88

1036 Cashman, K. V., & Scheu, B. (2015). Magmatic fragmentation. In The encyclopedia of volcanoes (pp.
1037 459-471). Academic Press. doi:10.1016/B978-0-12-385938-9.00025-0

1038 Cesca, S., Letort, J., Razafindrakoto, H. N., Heimann, S., Rivalta, E., Isken, M. P., ... & Dahm, T. (2020).
1039 Drainage of a deep magma reservoir near Mayotte inferred from seismicity and deformation. Nature
1040 geoscience, 13(1), 87-93. doi:10.1038/s41561-019-0505-5

1041 Coffin, M. F., & Rabinowitz, P. D. (1987). Reconstruction of Madagascar and Africa: evidence from the
1042 Davie fracture zone and western Somali basin. Journal of Geophysical Research: Solid Earth, 92(B9),
1043 9385-9406. doi:10.1029/JB092iB09p09385

1044 Colombier, M., Scheu, B., Kueppers, U., Cronin, S., Mueller, S., Hess, K.-U., Dingwell, D. B. (2019a). In
1045 situ granulation by thermal stress during subaqueous volcanic eruptions. Geology, 47(2), 179–182.
1046 doi:10.1130/g45503.1

1047 Colombier, M., Mueller, S. B., Kueppers, U., Scheu, B., Delmelle, P., Cimarelli, C., ... & Dingwell, D. B.
1048 (2019b). Diversity of soluble salt concentrations on volcanic ash aggregates from a variety of eruption
1049 types and deposits. Bulletin of Volcanology, 81(7), 1-13. doi:10.1007/s00445-019-1302-0

1050 Costantini, L., Houghton, B. F., & Bonadonna, C. (2010). Constraints on eruption dynamics of basaltic
1051 explosive activity derived from chemical and microtextural study: the example of the Fontana Lapilli
1052 Plinian eruption, Nicaragua. Journal of Volcanology and Geothermal Research, 189(3-4), 207-224.
1053 doi:10.1016/j.jvolgeores.2009.11.008

1054 Dellino, P., Gudmundsson, M. T., Larsen, G., Mele, D., Stevenson, J. A., Thordarson, T., & Zimanowski,
1055 B. (2012). Ash from the Eyjafjallajökull eruption (Iceland): Fragmentation processes and aerodynamic
1056 behavior. Journal of Geophysical Research: Solid Earth, 117(B9). doi:10.1029/2011JB008726

1057 Desgrolard, F. (1996). Pétrologie des laves d'un volcan intraplaque océanique : le Karthala, Ile de la
1058 Grande Comore – (R.F.I. des Comores). PhD Thesis, University Joseph Fourier, Grenoble 1, 176 p. +
1059 annexes

1060 Dingwell, D. B. (1996). Volcanic Dilemma--Flow or Blow? Science, 273(5278), 1054–1055.
1061 doi:10.1126/science.273.5278.1054

1062 Dille, A., Poppe, S., Mossoux, S., Soulé, H., & Kervyn, M. (2020). Modeling Lahars on a Poorly Eroded
1063 Basaltic Shield: Karthala Volcano, Grande Comore Island. Frontiers in Earth Science, 8.
1064 doi:10.3389/feart.2020.00369

1065 Doubik, P., & Hill, B. E. (1999). Magmatic and hydromagmatic conduit development during the 1975
1066 Tolbachik Eruption, Kamchatka, with implications for hazards assessment at Yucca Mountain, NV.
1067 Journal of Volcanology and Geothermal Research, 91(1), 43–64. doi:10.1016/s0377-0273(99)00052-9

1068 Dürig, T., Mele, D., Dellino, P., & Zimanowski, B. (2012a). Comparative analyses of glass fragments
1069 from brittle fracture experiments and volcanic ash particles. Bulletin of volcanology, 74(3), 691-704.
1070 doi:10.1007/s00445-011-0562-0

1071 Dürig, T., Sonder, I., Zimanowski, B., Beyrichen, H., & Büttner, R. (2012b). Generation of volcanic ash
1072 by basaltic volcanism. Journal of Geophysical Research: Solid Earth, 117(B1).
1073 doi:10.1029/2011JB008628

1074 Dvorak, J. J. (1992). Mechanism of explosive eruptions of Kilauea Volcano, Hawaii. Bulletin of
1075 volcanology, 54(8), 638-645. doi:10.1007/BF00430777

1076 Dzurisin, D., Lockwood, J. P., Casadevall, T. J., & Rubin, M. (1995). The Uwekahuna Ash Member of
1077 the Puna Basalt: product of violent phreatomagmatic eruptions at Kilauea volcano, Hawaii, between
1078 2800 and 210014C years ago. Journal of Volcanology and Geothermal Research, 66(1-4), 163-184.
1079 doi:10.1016/0377-0273(94)00062-L

1080 Edwards, M. J., Pioli, L., Harris, A. J., Gurioli, L., & Thivet, S. (2020). Magma fragmentation and particle
1081 size distributions in low intensity mafic explosions: the July/August 2015 Piton de la Fournaise
1082 eruption. Scientific reports, 10(1), 1-14. doi:10.1038/s41598-020-69976-y

1083 Emerick, C. M., & Duncan, R. A. (1982). Age progressive volcanism in the Comores Archipelago,
1084 western Indian Ocean and implications for Somali plate tectonics. Earth and Planetary Science
1085 Letters, 60(3), 415–428. doi:10.1016/0012-821x(82)90077-2

1086 Eychenne, J., Le Pennec, J. L., Troncoso, L., Gouhier, M., & Nedelec, J. M. (2012). Causes and
1087 consequences of bimodal grain-size distribution of tephra fall deposited during the August 2006
1088 Tungurahua eruption (Ecuador). Bulletin of Volcanology, 74(1), 187-205. doi:10.1007/s00445-011-
1089 0517-5

1090 Famin, V., Michon, L., & Bourhane, A. (2020). The Comoros archipelago: a right-lateral transform
1091 boundary between the Somalia and Lwandle plates. Tectonophysics, 789, 228539.
1092 doi:10.1016/j.tecto.2020.228539

1093 Feuillet, N., Jorry, S., Crawford, W.C., Deplus, C., Thinon, I., Jacques, … & Van der Woerd, J. (2021).
1094 Birth of a large volcanic edifice offshore Mayotte via lithosphere-scale dyke intrusion. Nature. Geosci.
1095 https://doi.org/10.1038/s41561-021-00809-x.

1096 Fitch, E. P., & Fagents, S. A. (2020). Characteristics of rootless cone tephra emplaced by high-energy
1097 lava–water explosions. Bulletin of Volcanology, 82(8), 1-16. doi:10.1007/s00445-020-01393-5

1098 Flower, M. F. J., & Strong, D. F. (1969). The significance of sandstone inclusions in lavas of the
1099 comores archipelago. Earth and Planetary Science Letters, 7(1), 47–50. doi:10.1016/0012-
1100 821x(69)90010-7

1101 Frazzetta, G., La Volpe, L., & Sheridan, M. F. (1983). Evolution of the Fossa cone, Vulcano. Journal of
1102 Volcanology and Geothermal Research, 17(1-4), 329-360. doi:10.1016/0377-0273(83)90075-6

1103 Gaudin, D., Taddeucci, J., Scarlato, P., Harris, A., Bombrun, M., Del Bello, E., & Ricci, T. (2017).
1104 Characteristics of puffing activity revealed by ground-based, thermal infrared imaging: the example
1105 of Stromboli Volcano (Italy). Bulletin of Volcanology, 79(3), 24. doi:10.1007/s00445-017-1108-x

1106 Giordano, D., Russell, J. K., & Dingwell, D. B. (2008). Viscosity of magmatic liquids: a model. Earth and
1107 Planetary Science Letters, 271(1-4), 123-134. doi:10.1016/j.epsl.2008.03.038

1108 Giordano, D., & Dingwell, D. (2003). Viscosity of hydrous Etna basalt: implications for Plinian-style
1109 basaltic eruptions. Bulletin of Volcanology, 65(1), 8-14. doi:10.1007/s00445-002-0233-2

1110 Gonnermann, Helge M., and Michael Manga. "Dynamics of magma ascent." Modeling volcanic
1111 processes: The physics and mathematics of volcanism (2013): 55-84.
1112 doi:10.1017/CBO9781139021562.004

1113 Graettinger, A. H., Skilling, I., McGarvie, D., Höskuldsson, A. (2013). Subaqueous basaltic magmatic
1114 explosions trigger phreatomagmatism: A case study from Askja, Iceland. Journal of Volcanology and
1115 Geothermal Research, 264, 17–35. doi:10.1016/j.jvolgeores.2013.08.001

1116 Gudmundsson, M. T., Thordarson, T., Höskuldsson, Á., Larsen, G., Björnsson, H., Prata, F. J., ... &
1117 Jónsdóttir, I. (2012). Ash generation and distribution from the April-May 2010 eruption of
1118 Eyjafjallajökull, Iceland. Scientific reports, 2(1), 1-12. doi:10.1038/srep00572

1119 Gurioli, L., Muro, A. D., Vlastélic, I., Moune, S., Thivet, S., Valer, M., ... & Hénot, J. M. (2018).
1120 Integrating field, textural, and geochemical monitoring to track eruption triggers and dynamics: a
1121 case study from Piton de la Fournaise. Solid Earth, 9(2), 431-455. doi:10.5194/se-9-431-2018, 2018.

1122 Gurioli, L., Colo', L., Bollasina, A. J., Harris, A. J., Whittington, A., & Ripepe, M. (2014). Dynamics of
1123 Strombolian explosions: inferences from field and laboratory studies of erupted bombs from
1124 Stromboli volcano. Journal of Geophysical Research: Solid Earth, 119(1), 319-345.
1125 doi:10.1002/2013JB010355

1126 Head, J. W., & Wilson, L. (1987). Lava fountain heights at Pu'u'O'o, Kilauea, Hawaii: Indicators of
1127 amount and variations of exsolved magma volatiles. Journal of Geophysical Research: Solid Earth,
1128 92(B13), 13715-13719. doi:10.1029/JB092iB13p13715

1129 Heiken, G., Wohletz, K. (1987). Tephra deposits associated with silicic domes and lava flows. The
1130 Emplacement of Silicic Domes and Lava Flows. doi:10.1130/SPE212-p55

1131 Houghton, B., White, J. D., & Van Eaton, A. R. (2015). Phreatomagmatic and related eruption styles.
1132 In The encyclopedia of volcanoes (pp. 537-552). Academic Press. doi:10.1016/B978-0-12-385938-
1133 9.00030-4

1134 Houghton, B. F., Wilson, C. J. N., Rosenberg, M. D., Smith, I. E. M., & Parker, R. J. (1996). Mixed
1135 deposits of complex magmatic and phreatomagmatic volcanism: an example from Crater Hill,
1136 Auckland, New Zealand. Bulletin of Volcanology, 58(1), 59–66. doi:10.1007/s004450050126

1137 Jenkins, S. F., Wilson, T. M., Magill, C., Miller, V., Stewart, C., Blong, R., ... & Costa, A. (2015). Volcanic
1138 ash fall hazard and risk. Global volcanic hazards and risk, 173-222.
1139 doi:10.1017/CBO9781316276273.005

1140 Jordan, S. C., Le Pennec, J. L., Gurioli, L., Roche, O., & Boivin, P. (2016). Highly explosive eruption of
1141 the monogenetic 8.6 ka BP La Vache et Lassolas scoria cone complex (Chaîne des Puys, France).
1142 Journal of Volcanology and Geothermal Research, 313, 15-28. doi:10.1016/j.jvolgeores.2015.12.006

1143 Krafft, M. (1982). L'éruption volcanique du Kartala : avril 1977 (Grande Comore, Ocean Indien),
1144 Compte rendu Académie des Sciences de Paris v294, n2: 753-758

1145 Lange, R. A., Frey, H. M., & Hector, J. (2009). A thermodynamic model for the plagioclase-liquid
1146 hygrometer/thermometer. American Mineralogist, 94(4), 494-506. doi:10.2138/am.2009.3011

1147 Latutrie, B., & Ross, P.-S. (2020). Phreatomagmatic vs magmatic eruptive styles in maar-diatremes: a
1148 case study at Twin Peaks, Hopi Buttes volcanic field, Navajo Nation, Arizona. Bulletin of Volcanology,
1149 82(3). doi:10.1007/s00445-020-1365-y

1150 Leibrandt, S., & Le Pennec, J. L. (2015). Towards fast and routine analyses of volcanic ash
1151 morphometry for eruption surveillance applications. Journal of Volcanology and Geothermal
1152 Research, 297, 11-27. doi:10.1016/j.jvolgeores.2015.03.014

1153 Lemoine, A., Briole, P., Bertil, D., Roullé, A., Foumelis, M., Thinon, I., ... & Hoste Colomer, R. (2020).
1154 The 2018–2019 seismo-volcanic crisis east of Mayotte, Comoros islands: seismicity and ground
1155 deformation markers of an exceptional submarine eruption. Geophysical Journal International,
1156 223(1), 22-44. doi:10.1093/gji/ggaa273

1157 Lénat, J.-F., Robineau, B., Durand, S., & Bachèlery, P. (1998). Étude de la zone sommitale du volcan
1158 Karthala (Grande Comore) par polarisation spontanée. Comptes Rendus de l'Académie Des Sciences -
1159 Series IIA - Earth and Planetary Science, 327(12), 781–788. doi:10.1016/s1251-8050(99)80051-2

1160 Lipman, P. W., Banks, N. G., & Rhodes, J. M. (1985). Degassing-induced crystallization of basaltic
1161 magma and effects on lava rheology. Nature, 317(6038), 604-607. doi:10.1038/317604a0

1162 Liu, E. J., Cashman, K. V., Rust, A. C. & Gislason, S. R. (2015). The role of bubbles in generating fine ash
1163 during hydromagmatic eruptions. Geology, 43(3), 239–242. doi:10.1130/G36336.1

1164 Liuzzo, M., Di Muro, A., Rizzo, A. L., Caracausi, A., Grassa, F., Fournier, N., Shafik, B., Boudoire, G.,
1165 Coltorti, M., Moreira, M., & Italiano, F. (2021). Gas geochemistry at Grande Comore and Mayotte
1166 volcanic islands (Comoros archipelago), Indian ocean. Earth and Space Science Open Archive, Journal
1167 article DP. doi:10.1002/essoar.10506929.1

1168 Llewellin, E. W., & Manga, M. (2005). Bubble suspension rheology and implications for conduit flow.
1169 Journal of Volcanology and Geothermal Research, 143(1-3), 205-217.
1170 doi:10.1016/j.jvolgeores.2004.09.018

1171 Mader, H. M., Llewellin, E. W., & Mueller, S. P. (2013). The rheology of two-phase magmas: A review
1172 and analysis. Journal of Volcanology and Geothermal Research, 257, 135-158.
1173 doi:10.1016/j.jvolgeores.2013.02.014

1174 Magnússon, E., Gudmundsson, M. T., Roberts, M. J., Sigurðsson, G., Höskuldsson, F., & Oddsson, B.
1175 (2012). Ice-volcano interactions during the 2010 Eyjafjallajökull eruption, as revealed by airborne
1176 imaging radar. Journal of Geophysical Research: Solid Earth, 117(B7). doi:10.1029/2012JB009250

1177 Maron, S. H., & Pierce, P. E. (1956). Application of Ree-Eyring generalized flow theory to suspensions
1178 of spherical particles. Journal of colloid science, 11(1), 80-95. doi:10.1016/0095-8522(56)90023-X

1179 Mastin, L. G. (2007). Generation of fine hydromagmatic ash by growth and disintegration of glassy
1180 rinds. Journal of Geophysical Research, 112(B2). doi:10.1029/2005jb003883

1181 Mastin, L. G., & Witter, J. B. (2000). The hazards of eruptions through lakes and seawater. Journal of
1182 Volcanology and Geothermal Research, 97(1-4), 195–214. doi:10.1016/s0377-0273(99)00174-2

1183 McPhie, J., Walker, G. P., & Christiansen, R. L. (1990). Phreatomagmatic and phreatic fall and surge
1184 deposits from explosions at Kilauea volcano, Hawaii, 1790 AD: Keanakakoi Ash Member. Bulletin of
1185 Volcanology, 52(5), 334-354. doi:10.1007/BF00302047

1186 Métrich, N., Bertagnini, A., & Di Muro, A. (2010). Conditions of Magma Storage, Degassing and
1187 Ascent at Stromboli: New Insights into the Volcano Plumbing System with Inferences on the Eruptive
1188 Dynamics. Journal of Petrology, 51(3), 603–626. doi:10.1093/petrology/egp083

1189 Métrich, N., Bertagnini, A., Landi, P., Rosi, M., & Belhadj, O. (2005). Triggering mechanism at the
1190 origin of paroxysms at Stromboli (Aeolian Archipelago, Italy): the 5 April 2003 eruption. Geophysical
1191 Research Letters, 32(10). doi:10.1029/2004GL022257

1192 Michon L. (2016). The Volcanism of the Comoros Archipelago Integrated at a Regional Scale. Active
1193 Volcanoes of the Southwest Indian Ocean. Active Volcanoes of the World. Springer, Berlin,
1194 Heidelberg. doi:10.1007/978-3-642-31395-0_21

1195 Michon, L., Di Muro, A., Villeneuve, N., Saint-Marc, C., Fadda, P., & Manta, F. (2013). Explosive
1196 activity of the summit cone of Piton de la Fournaise volcano (La Réunion island): a historical and
1197 geological review. Journal of Volcanology and Geothermal Research, 264, 117-133.
1198 doi:10.1016/j.jvolgeores.2013.06.012

1199 Morin J., Bachèlery P., Soulé H., Nassor H. (2016). Volcanic Risk and Crisis Management on Grande
1200 Comore Island. Active Volcanoes of the Southwest Indian Ocean. Active Volcanoes of the World.
1201 Springer, Berlin, Heidelberg. doi:10.1007/978-3-642-31395-0_25

1202 Morin, J., Lavigne, F., Bachelery, P., Finizola, A., & Villeneuve, N. (2009). Institutional and social
1203 responses to hazards related to Karthala volcano, Comoros. Shima: The international journal of
1204 research into Island cultures, 3(1), 55-71

1205 Montanaro, C., Cronin, S. J., Scheu, B., Kennedy, B., Scott, B. J., & Dingwell, D. B. (2021). Host Rock
1206 Variability Powers the Diversity of Steam-Driven Eruptions. Geophysical Research Letters, 48(1),
1207 e2020GL089025. doi:10.1029/2020GL089025

1208 Nassor, H. (2001). Contribution à l'étude du risque volcanique sur les grands volcans boucliers
1209 basaltiques: le Karthala et le Piton de la Fournaise. PhD thesis, University of La Réunion

1210 Németh, K., & Kósik, S. (2020). Review of explosive hydrovolcanism. Geosciences, 10(2), 44.
1211 doi:10.3390/geosciences10020044

1212 Nougier, J., Cantagrel, J. M., & Karche, J. P. (1986). The Comores archipelago in the western Indian
1213 Ocean: volcanology, geochronology and geodynamic setting. Journal of African Earth Sciences (1983),
1214 5(2), 135–145. doi:10.1016/0899-5362(86)90003-5

1215 Ort, M. H., & Carrasco-Núñez, G. (2009). Lateral vent migration during phreatomagmatic and
1216 magmatic eruptions at Tecuitlapa Maar, east-central Mexico. Journal of Volcanology and Geothermal
1217 Research, 181(1-2), 67-77. doi:10.1016/j.jvolgeores.2009.01.003

1218 Papale, P. (1999). Strain-induced magma fragmentation in explosive eruptions. Nature, 397(6718),
1219 425–428. doi:10.1038/17109

1220 Parcheta, C. E., Houghton, B. F., & Swanson, D. A. (2013). Contrasting patterns of vesiculation in low,
1221 intermediate, and high Hawaiian fountains: a case study of the 1969 Mauna Ulu eruption. Journal of
1222 Volcanology and Geothermal Research, 255, 79-89. doi:10.1016/j.jvolgeores.2013.01.016

1223 Parfitt, E. A. (1998). A study of clast size distribution, ash deposition and fragmentation in a
1224 Hawaiian-style volcanic eruption. Journal of Volcanology and Geothermal Research, 84(3-4), 197–
1225 208. doi:10.1016/s0377-0273(98)00042-0

1226 Pedersen, G. B. M., Höskuldsson, A., Dürig, T., Thordarson, T., Jonsdottir, I., Riishuus, M. S., ... &
1227 Schmith, J. (2017). Lava field evolution and emplacement dynamics of the 2014–2015 basaltic fissure
1228 eruption at Holuhraun, Iceland. Journal of Volcanology and Geothermal Research, 340, 155-169.
1229 doi:10.1016/j.jvolgeores.2017.02.027

1230 Pioli, L., Erlund, E., Johnson, E., Cashman, K., Wallace, P., Rosi, M., & Granados, H. D. (2008).
1231 Explosive dynamics of violent Strombolian eruptions: the eruption of Parícutin Volcano 1943–1952
1232 (Mexico). Earth and Planetary Science Letters, 271(1-4), 359-368. doi:10.1016/j.epsl.2008.04.026

1233 Polacci, M., Corsaro, R. A., & Andronico, D. (2006). Coupled textural and compositional
1234 characterization of basaltic scoria: Insights into the transition from Strombolian to fire fountain
1235 activity at Mount Etna, Italy. Geology, 34(3), 201-204. doi:10.1130/G22318.1

1236 Poppe, S. (2012). Caldera collapse on basaltic shield volcanoes: analogue models compared to the
1237 Karthala caldera complex, Grande Comore. MSc report, Ghent University, Belgium

1238 Prata, A. J., & Kerkmann, J. (2007). Simultaneous retrieval of volcanic ash and SO2 using MSG-SEVIRI
1239 measurements. Geophysical Research Letters, 34(5). doi:10.1029/2006GL028691

1240 Ross, P. S., Dürig, T., Comida, P. P., Lefebvre, N., White, J. D., Andronico, D., ... & Gurioli, L. (2022).
1241 Standardized analysis of juvenile pyroclasts in comparative studies of primary magma fragmentation;
1242 1. Overview and workflow. Bulletin of Volcanology, 84(1), 1-29. doi:10.1007/s00445-021-01516-6

1243 Sable, J. E., Houghton, B., Wilson, C. J. N., & Carey, R. J. (2009). Eruption mechanisms during the
1244 climax of the Tarawera 1886 basaltic Plinian eruption inferred from microtextural. Studies in
1245 volcanology: the legacy of George Walker, (2), 129. doi:10.1144/IAVCEl002.7

1246 Sable, J. E., Houghton, B. F., Del Carlo, P., & Coltelli, M. (2006). Changing conditions of magma ascent
1247 and fragmentation during the Etna 122 BC basaltic Plinian eruption: Evidence from clast
1248 microtextures. Journal of Volcanology and Geothermal Research, 158(3-4), 333-354.
1249 doi:10.1016/j.jvolgeores.2006.07.006

1250 Savin, C., Grasso, J.-R., & Bachelery, P. (2005). Seismic signature of a phreatic explosion:
1251 hydrofracturing damage at Karthala volcano, Grande Comore Island, Indian Ocean. Bulletin of
1252 Volcanology, 67(8), 717–731. doi:10.1007/s00445-005-0411-0

1253 Savin, C., Ritz, M., Join, J.-L., & Bachelery, P. (2001). Hydrothermal system mapped by CSAMT on
1254 Karthala volcano, Grande Comore Island, Indian Ocean. Journal of Applied Geophysics, 48(3), 143–
1255 152. doi:10.1016/s0926-9851(01)00078-7

1256 Self, S., Kienle, J., & Huot, J. P. (1980). Ukinrek Maars, Alaska, II. Deposits and formation of the 1977
1257 craters. Journal of Volcanology and Geothermal Research, 7(1-2), 39-65. doi:10.1016/0377-
1258 0273(80)90019-0

1259 Shea, T. (2017). Bubble nucleation in magmas: a dominantly heterogeneous process?. Journal of
1260 Volcanology and Geothermal Research, 343, 155-170. doi:10.1016/j.jvolgeores.2017.06.025

1261 Shea, T., Houghton, B. F., Gurioli, L., Cashman, K. V., Hammer, J. E., & Hobden, B. J. (2010). Textural
1262 studies of vesicles in volcanic rocks: an integrated methodology. Journal of Volcanology and
1263 Geothermal Research, 190(3-4), 271-289. doi:10.1016/j.jvolgeores.2009.12.003

1264 Sheridan, M. F., & Wohletz, K. H. (1983). Hydrovolcanism: basic considerations and review. Journal of
1265 Volcanology and Geothermal Research, 17(1-4), 1-29. doi:10.1016/0377-0273(83)90060-4

1266 Siebert, L., Cottrell, E., Venzke, E., & Andrews, B. (2015). Earth's volcanoes and their eruptions: An
1267 overview. The encyclopedia of volcanoes, 239-255. doi:10.1016/B978-0-12-385938-9.00012-2

1268 Small, C., & Naumann, T. (2001). The global distribution of human population and recent volcanism.
1269 Global Environmental Change Part B: Environmental Hazards, 3(3), 93-109.
1270 doi:10.3763/ehaz.2001.0309

1271 Smietana, M. (2007). Etude pétrologique et volcanologique des dépôts des quatre dernières
1272 éruptions du Karthala. MSc report, University of La Réunion, France, 51.

1273 Staudacher, T., Ferrazzini, V., Peltier, A., Kowalski, P., Boissier, P., Catherine, P., ... & Massin, F.
1274 (2009). The April 2007 eruption and the Dolomieu crater collapse, two major events at Piton de la
1275 Fournaise (La Réunion Island, Indian Ocean). Journal of Volcanology and Geothermal Research,
1276 184(1-2), 126-137. doi:10.1016/j.jvolgeores.2008.11.005

1277 Stovall, W. K., Houghton, B. F., Gonnermann, H., Fagents, S. A., & Swanson, D. A. (2011). Eruption
1278 dynamics of Hawaiian-style fountains: the case study of episode 1 of the Kīlauea Iki 1959 eruption.
1279 Bulletin of Volcanology, 73(5), 511-529. doi:10.1007/s00445-010-0426-z

1280 Strong, D. F., & Jacquot, C. (1970). The Karthala caldera, Grande Comore. Bulletin Volcanologique,
1281 34(3), 663–680. doi:10.1007/bf02596697

1282 Tanner, W. F. (1969). The particle size scale. Journal of Sedimentary Research, 39(2), 809-812.
1283 doi:10.1306/74D71D39-2B21-11D7-8648000102C1865D

1284 Taddeucci, J., Edmonds, M., Houghton, B., James, M. R., & Vergniolle, S. (2015). Hawaiian and
1285 Strombolian eruptions. In The encyclopedia of volcanoes (pp. 485-503). Academic Press.
1286 doi:10.1016/B978-0-12-385938-9.00027-4

1287 Thiéry, R., & Mercury, L. (2009). Explosive properties of water in volcanic and hydrothermal systems.
1288 Journal of Geophysical Research, 114(B5). doi:10.1029/2008jb005742

1289 Thivet, S., Harris, A. J., Gurioli, L., Bani, P., Barnie, T., Bombrun, M., & Marchetti, E. (2021). Multi-
1290 parametric field experiment links explosive activity and persistent degassing at Stromboli. Frontiers
1291 in Earth Science, 9, 431. doi: 10.3389/feart.2021.669661

1292 Thivet, S., Gurioli, L., Di Muro, A., Derrien, A., Ferrazzini, V., Gouhier, M., ... & Arellano, S. (2020a).
1293 Evidences of plug pressurization enhancing magma fragmentation during the September 2016
1294 basaltic eruption at Piton de la Fournaise (La Réunion Island, France). Geochemistry, Geophysics,
1295 Geosystems, 21(2). doi:10.1029/2019GC008611

1296 Thivet, S., Gurioli, L., & Di Muro, A. (2020b). Basaltic dyke eruptions at Piton de La Fournaise:
1297 characterization of the eruptive products with implications for reservoir conditions, conduit
1298 processes and eruptive dynamics. Contributions to Mineralogy and Petrology, 175(3), 1-24.
1299 doi:10.1007/s00410-020-1664-5

1300 Thivet, S., Gurioli, L., Di Muro, A., Eychenne, J., Besson, P., & Nedelec, J. M. (2020c). Variability of ash
1301 deposits at Piton de la Fournaise (La Reunion Island): insights into fragmentation processes at
1302 basaltic shield volcanoes. Bulletin of Volcanology, 82(9), 1-20. doi:10.1007/s00445-020-01398-0

1303 Thordarson, T., Larsen, G. (2007). Volcanism in Iceland in historical time: Volcano types, eruption
1304 styles and eruptive history. Journal of Geodynamics, 43(1), 0–152. doi:10.1016/j.jog.2006.09.005

1305 Toramaru, A. (2006). BND (bubble number density) decompression rate meter for explosive volcanic
1306 eruptions. Journal of Volcanology and Geothermal Research, 154(3-4), 303-316.
1307 doi:10.1016/j.jvolgeores.2006.03.027

1308 Truby, J. M., Mueller, S. P., Llewellin, E. W., & Mader, H. M. (2015). The rheology of three-phase
1309 suspensions at low bubble capillary number. Proceedings of the Royal Society A: Mathematical,
1310 Physical and Engineering Sciences, 471(2173), 20140557. doi:10.1098/rspa.2014.0557

1311 Tzevahirtzian, A., Zaragosi, S., Bachèlery, P., Biscara, L., & Marchès, E. (2021). Submarine morphology
1312 of the Comoros volcanic archipelago. Mar. Geol. 432. doi:10.1016/j.margeo.2020.106383.

1313 Van der Plas, L., & Tobi, A. C. (1965). A chart for judging the reliability of point counting results.
1314 American Journal of Science, 263(1), 87-90. doi:10.2475/ajs.263.1.87

1315 Vergniolle, S., & Gaudemer, Y. (2012). Decadal evolution of a degassing magma reservoir unravelled
1316 from fire fountains produced at Etna volcano (Italy) between 1989 and 2001. Bulletin of volcanology,
1317 74(3), 725-742. doi:10.1007/s00445-011-0563-z

1318 White, J. D., & Valentine, G. A. (2016). Magmatic versus phreatomagmatic fragmentation: Absence of
1319 evidence is not evidence of absence. Geosphere, 12(5), 1478-1488. doi:10.1130/GES01337.1

1320 White, J. D., Schipper, C. I., & Kano, K. (2015). Submarine explosive eruptions. In The encyclopedia of
1321 volcanoes (pp. 553-569). Academic Press. doi:10.1016/B978-0-12-385938-9.00031-6

1322 White, J. D. L., & Houghton, B. F. (2006). Primary volcaniclastic rocks. Geology, 34(8), 677-680.
1323 doi:10.1130/G22346.1

1324 Wohletz, K., Zimanowski, B., & Büttner, R. (2013). Magma-water interactions. Modeling volcanic
1325 processes, 230-256. doi:10.1017/CBO9781139021562.011

1326 Wohletz, K. H., & McQueen, R. G. (1984). Volcanic and stratospheric dustlike particles produced by
1327 experimental water-melt interactions. Geology, 12(10), 591-594. doi:10.1130/0091-
1328 7613(1984)12<591:VASDPP>2.0.CO;2

1329 Zhang, Y. (1999). A criterion for the fragmentation of bubbly magma based on brittle failure theory.
1330 Nature 402, 648–650.doi:10.1038/45210

1331 Xu, Z., & Zhang, Y. (2002). Quench rates in air, water, and liquid nitrogen, and inference of
1332 temperature in volcanic eruption columns. Earth and Planetary Science Letters, 200(3-4), 315-330.
1333 doi: 10.1016/S0012-821X(02)00656-8

1334 Zimanowski, B., Büttner, R., Dellino, P., White, J. D., & Wohletz, K. H. (2015). Magma–water
1335 interaction and phreatomagmatic fragmentation. In The encyclopedia of volcanoes (pp. 473-484).
1336 Academic Press. doi:10.1016/B978-0-12-385938-9.00026-2